Spring 5-2021

# Analysis of Fluid Flow in Redox Flow Batteries

Erfan asadipour
*Washington University in St. Louis*

Washington University in St. Louis
McKelvey School of Engineering
Department of Energy, Environmental and Chemical Engineering

Thesis Examination Committee:
Dr. Vijay Ramani, Chair
Dr. Palghat Ramachandran
Dr. Benjamin Kumfer

# Analysis of fluid flow in redox flow batteries

By
Erfan Asadipour

A thesis presented to the McKelvey School of Engineering
of Washington University in St. Louis in partial fulfillment
of the requirements for the degree of

Master of Science

May 2021
St. Louis, Missouri

Acknowledgments

I would like to express my deepest gratitude to everyone who has been with me during my MSc studies at Washington University in St. Louis. It is a privilege to work in an engaging environment, helping students to be more productive and mature. I cannot be more excited for my next journey at Washington University in St. Louis as a PhD student.

I am so grateful to Dr. Vijay Ramani. He is the true definition of an advisor: understanding and well-informed. He helped me gather myself while I was struggling the first semesters of my graduate studies and provided me with an opportunity to build my career in electrochemical engineering. He taught me how to be rigorous and grounded in my approach to research, and taught me the importance of communication and writing skills.

I am equally grateful to my thesis committee members, Dr. Palghat Ramachandran and Dr. Benjamin Kumfer, for the guidance they have given me throughout my MSc studies. Dr. Kumfer has been a great mentor from the first months I have joined Electrochemical Engineering Research Laboratory, and I hope I can use his advisory for the later steps of my career. I had gathered vast amount of knowledge in transport phenomena from attending Dr. Ramachandran's lectures and our personal meetings. He was a great mentor, and he will truly be missed.

I want to thank everyone in the Electrochemical Engineering Research Laboratory, current members and alumni. It has been a privilege to work alongside this team of brilliant researchers. I want to especially thank Dr. Shrihari Sankarasubramanian, Yunzhu Zhang, Jing Xie, and Kritika Sharma, as they have been the most influential in my journey throughout my MSc studies.

At last, I want to thank my parents, Farrokh Asadipour and Mozhgan Moradi Sarmeidani , and my lovely sister, Kimiya Asadipour, and many other family members and friends for their

unconditional love and tremendous support throughout the last three years. I thank Mrs. Narges Naemi and her family for their great support and love during my time in St. Louis.

Erfan Asadipour

Washington University in St. Louis

May 2021

Table of Contents

List of Figures

List of Tables

Nomenclature

| Symbols | Definition |
|---|---|
| RFB | Redox flow battery |
| IFF | Interdigitated flow field |
| SSFF | Single-channel serpentine flow field |
| MSFF | Multi-channels serpentine flow field |
| 3SFF | Three-channels serpentine flow field |
| PFF | Parallel flow field |
| FF | Flow field |
| SFF | Serpentine flow field |
| DN | Dimensionless number |
| HEAM | Hydraulic-electrical analogous model |
| HFB | Hybrid flow battery |
| IEM | Ion-exchange membrane |
| AEM | Anion-exchange membrane |
| CEM | Cation-exchange membrane |
| VRFB | All-vanadium redox flow battery |
| μ | Fluid dynamic viscosity |
| g | Gravitational constant |
| $E^0$ | Standard electric potential |
| SHE | Standard hydrogen electrode |
| ΔP | Pressure drop |

| Symbols | Definition |
|---|---|
| Q | Volumetric flow rate |
| $\eta$ | Efficiency |
| K, k | Permeability of the porous medium |
| w | Width |
| h | Height |
| L, l | Length |
| D, d | Diameter |
| Re | Reynolds number |
| Fr | Froude number |
| $\dot{m}$ | Mass flow rate |
| N-S | Navier-Stokes |
| A | Cross-sectional area |
| Eu | Euler number |
| $D_h$, $d_h$ | Hydraulic diameter |
| V | Electric potential |
| I | Electric current |
| R | Resistance |
| $\nabla$ | Gradient |
| $\nabla^2$ | Laplacian |
| RHS | Right-hand side |
| CR | Compression Ratio |
| LHS | Left-hand side |

| Subscripts | Definition |
|---|---|
| x | x-direction (in Cartesian coordination) |
| y | y-direction (in Cartesian coordination) |
| z | z-direction (in Cartesian coordination) |
| c | Channel section of the RFB |
| p | Porous section of the RFB |
| pump | Pump |
| h | hydraulic |
| m | modified |
| RFB | Redox flow battery |
| e | Entrance region |
| in | Coming inside of the system |
| out | Going outside of the system |
| r | Flow field ribs |
| el | Electrical |
| v | Viscous |
| FF | Flow field |

Abstract of the Thesis

Analysis of Fluid Flow in Redox Flow Batteries

By

Erfan Asadipour

Master of Science in Energy, Environmental and Chemical Engineering

Washington University in St. Louis, 2021

Research Advisor: Professor Vijay Ramani

Redox flow batteries (RFB) hold great potential for large-scale stationary energy storage. However, their low energy density compared to other energy storage systems must improve for feasibility. Electrolyte flow distribution affects current density distribution and providing a uniform current density distribution is one way to improve RFB performance. Additionally, reducing the power consumption of the electrolytes' pump as a source of energy loss in RFB systems increases their efficiency. Investigating both subjects requires analysis of the fluid dynamics in RFB cells.

In this thesis, a novel, computationally cost-effective hydraulic-electrical analogous model (HEAM) was developed to study fluid dynamics by implementing scaling analysis on Navier-Stokes and Darcy's equations. The accuracy of the model was tested by comparing it to experimental data, and it proved to be more accurate than other similar models in the literature. HEAM demonstrated the deficiencies of flow distribution in interdigitated flow fields (IFF) and suggested that lower viscous resistance at the flow distribution manifold or higher resistance in the

parallel channels remedies the flow maldistribution. Further analysis showed that RFBs with IFFs need lower pump power to operate than those with serpentine flow fields (SFF) with similar properties. The HEAM may serve as an accurate tool for predicting the electrolyte flow behavior in RFB cells in future analyses. Moreover, this study indicates numerous ways to improve the electrolyte flow distribution of RFB cells with IFF and demonstrates the appeal of IFFs despite their complicated geometry and deficiencies for large-scale RFB applications.

# Chapter 1- Introduction

## 1.1- Redox flow batteries: Applications and challenges

Renewable energy sources generate about 11.3% of the electricity produced in USA. Solar and wind, as renewable energy sources, supply 34% of the USA renewable electricity produced, as Figure 1. 1 demonstrates. [1] The intermittency of solar and wind energy hinders their widespread growth and further implementation into the energy production sector. Solar energy is available during the day and wind energy is only feasible when wind speeds are sufficient to rotate the wind turbine's blades. However, the associated lower greenhouse gas emissions obtained when utilizing the above-mentioned renewable energy sources compared to other common energy sources drives continued research in this field. Lawrence Livermore National Library (LLNL) energy flow charts illustrate that the share of solar and wind energy generation increased from 2.16% in 2014 to 3.8% in 2019, projecting a 75% increase in their share. [1] The intermittency of these sources remains troublesome, despite their increased share in energy generation. Wind and solar power plants need to be coupled with electric energy storage devices that can charge when the power generation rate is higher than its consumption rate, and discharge when additional power is needed to meet the electrical grid demands. Batteries, including redox flow batteries (RFB), are possible solutions for providing stable energy storage for solar and wind power plants. [2][3]

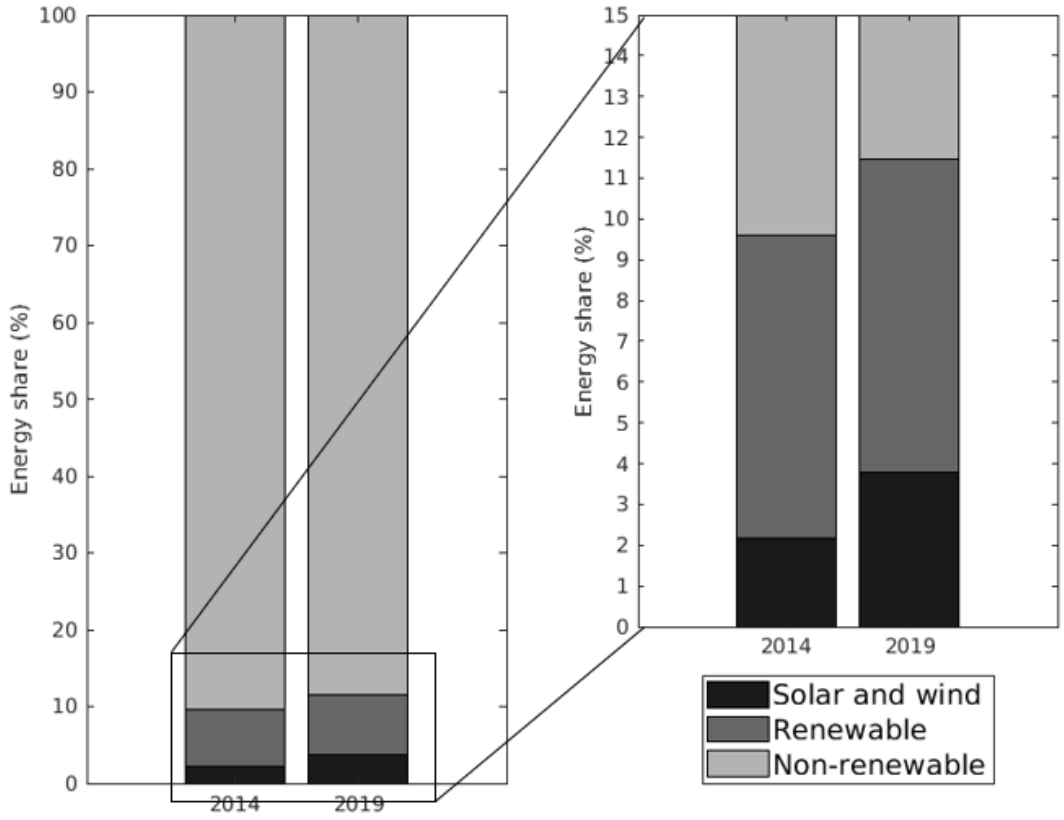


Figure 1. 1. Usage share of solar and wind energy, and other renewable and non-renewable energy sources in the energy production in USA at years 2014 and 2019. This graph shows an increase in the share of renewable energy sources, especially wind and solar during this timeframe. (Data are captured from [1])

Currently, energy storage technologies are too expensive to be integrated with wind and solar power plants. A recent report by the US Department of Energy (DOE) states that the average of total cost of current energy storage technologies varies between 450 and 1000 $/kWh. As shown in Figure 1. 2, this is more than the target cost of 100 $/kWh. [4] Currently, the cheapest energy storage technology is the Li-ion battery; however, the gap between RFBs and Li-ion batteries is closing. It is projected that in near future, RFBs can surpass the cost of Li-ion batteries, reach the

100 $/KWh cost goal for energy storage devices and be the first feasible grid-scale energy storage technology to be implemented with solar and wind power plants.

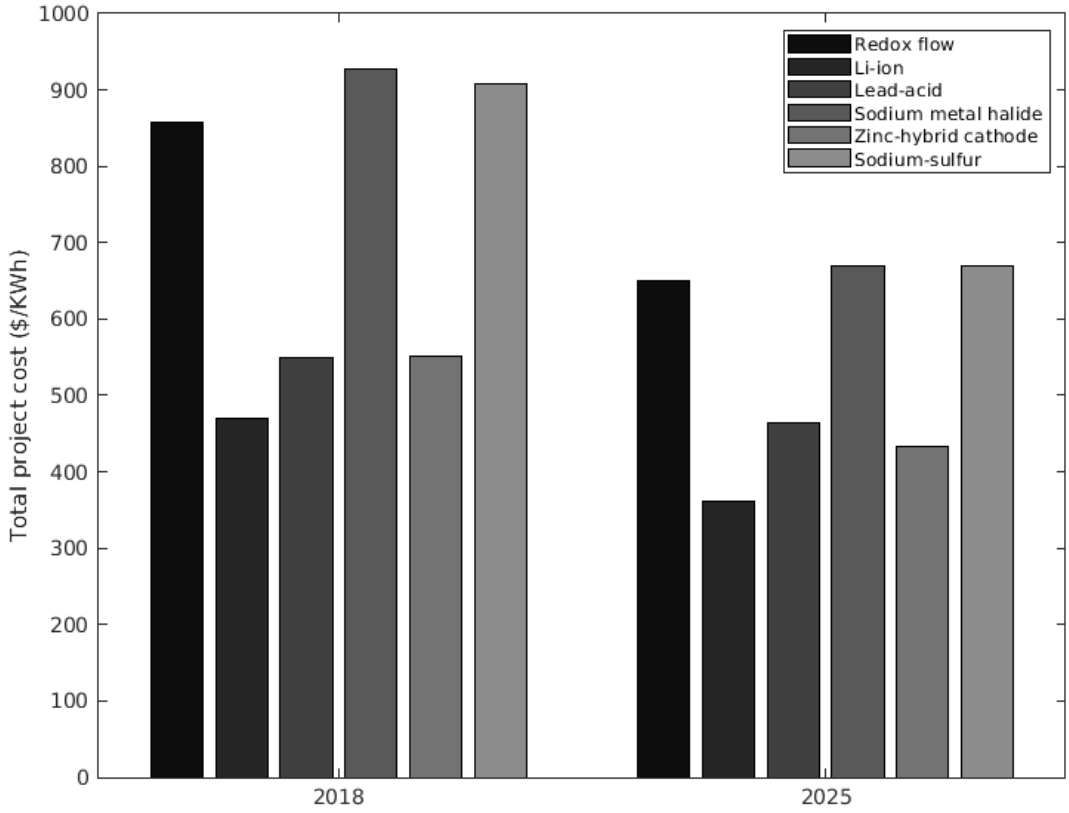


Figure 1. 2. Average of the total implementation project cost of various energy storage systems in 2018. The projected cost for the same systems in 2025 is also illustrated. Currently, the cheapest energy storage technology is the Li-ion battery. (The data are obtained from [4])

The advantages of RFB systems over other energy storage technologies include a longer lifetime (15~20 years compared to Li-ion battery's lifetime of 4~5 years), independent electrolyte storage and power unit, and convenient sizing of energy components. [2–4] However, they are expensive due to their low energy density, and high-cost active species. RFB systems also have non-uniform

flow, concentration, and current distribution due to their large sizes, which causes lower energy efficiency. [5]

## 1.2- All-vanadium redox flow batteries

Redox flow battery (RFB) consists of two electrolyte reservoirs, placed at the two sides of an electrochemical reactor, as shown in Figure 1. 3. Electrolytes are pumped continuously in and out of the reactor, forming reaction cycles. A fraction of reactants convert to products in each reaction cycle. For a cycle, the extent of each reaction depends on the residence time of the electrolytes in the reactor and the kinetics of the reactions. A specified ion is responsible for the exchange of electrons with the external electrical circuit on both sides of the electrochemical reactor; the ion-exchange membrane (IEM) allows that ion to pass and blocks other ions. Electrolytes are liquid solutions in flow batteries. Reactants and products are dissolved in electrolytes for RFBs, as opposed to hybrid flow batteries (HFBs), where multi-phase reactions occur and the presence of a solid-phase reactant is necessary for HFB operation. [2,6–8]

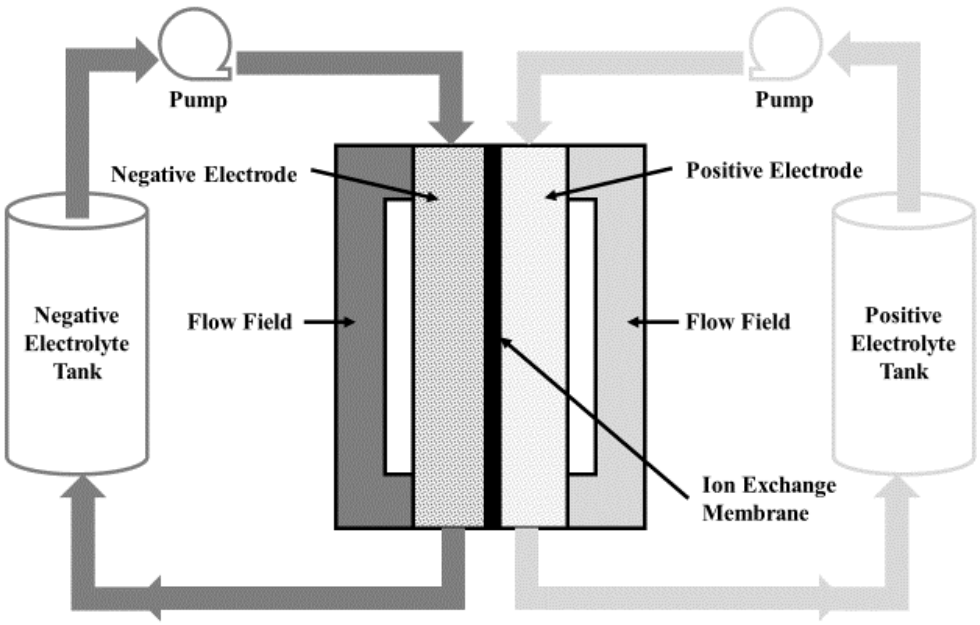

Figure 1. 3. A schematic of the fundamental operation of RFBs. Positive and negative electrolytes are pumped into the battery. Electrolytes passing through the electrodes trade electrons via an external circuit, alongside trading ions through the IEM.

All-vanadium redox flow batteries (VRFBs) are aqueous RFBs, which utilize four different states of vanadium ions for operation. VRFBs are the most studied RFBs, due to the simplicity of using various ions of one metal, instead of two or more base chemical compounds, as anode and cathode. Additionally, anions and cations are dissolved in the same solvent. Hence, the cell is stabilized by omitting the crossover of electrolytes; a problem occurring when employing different anolytes and catholytes. [2,5,9] The common solvent is diluted aqueous sulfuric acid for VRFBs. However, the dissolution of vanadium salt is limited to 1.7 M in this solvent, limiting the energy density of VRFBs. A couple of studies have suggested various additives for improving the solubility of vanadium up to 3 M, which leads to more energy-dense VRFBs. [3,10]

The electrochemical reactions of VRFBs are presented in Equations 1.1 and 1.2 for positive and negative electrodes. As deduced from these equations, the open circuit potential is 1.26V.

$$\text{Positive: } VO_2^+ + 2H^+ + e^- \leftrightarrow VO^{2+} + H_2O, E^0 = 1.0\ \text{V vs. SHE} \quad (1.1)$$

$$\text{Negative: } V^{3+} + e^- \leftrightarrow V^{2+}, E^0 = -0.26\ \text{V vs. SHE} \quad (1.2)$$

$VO^{2+}$ ions are oxidized to $VO_2^+$ ions in the positive half-cell reaction, and $V^{3+}$ ions are reduced to $V^{2+}$ ions in the negative half-cell reaction during the charging cycle. In other words, these ions transform into their more unstable states with higher energy differences by storing energy or being "charged". The unstable ions $VO_2^+$ and $V^{2+}$ take their more stable forms, $VO^{2+}$ and $V^{3+}$, respectively, during the discharging cycle. during this process, energy stored in the ions is released or the cell is "discharged".

The voltage required to run charging and discharging cycles is the same as the open circuit potential from thermodynamic point of view. However, applying the open circuit voltage does not run the cycles in practical applications, as kinetics of redox reactions require more voltage for charging and loss of voltage while discharging. The difference in applied voltage and open circuit potential is called overpotential. Butler-Volmer equation is the classic one to describe the kinetics of redox reactions: [11]

$$i = i_0 \left\{ \exp\left(\frac{\alpha_a n F \eta_s}{RT}\right) - \exp\left(-\frac{\alpha_c n F \eta_s}{RT}\right) \right\}, i_0 = A \exp\left(-\frac{E_a}{RT}\right), \eta_s = V - U \qquad (1.3)$$

Where i, $i_0$, $\alpha_a$, $\alpha_c$, F, R, T, n, $E_a$, U, V, and $\eta_s$ are obtained current density, exchange-current density, anodic activity coefficient, cathodic activity coefficient, Faraday's constant, universal gas constant, temperature, number of electrons transferred, activation energy, open-circuit potential, applied voltage, and overpotential, respectively. Exchange-current density accounts for the rate of forward and reverse reactions at equilibrium, which is represented by an Arrhenius expression. Based on Butler-Volmer equation, the amount of overpotential dictates the kinetics of redox reactions. Higher temperature, lower activation energy and higher activity coefficient result to lower overpotential. Lowering overpotential is desirable due to lower power required to charge and higher power discharged from RFB cells. This improvement leads to higher voltage and energy efficiency.

As depicted in Figure 1. 4, a simple VRFB system consists of endplates, current collectors, flow field plates (FF), porous electrodes, gaskets, IEM, and inlet and outlet tubing. Endplates, tightened to each other by nuts and bolts, are responsible for aligning and contain all the other components of a VRFB cell. Furthermore, they provide a platform for installing inlet and outlet tubing, which allows electrolytes to flow in and out of the cell.

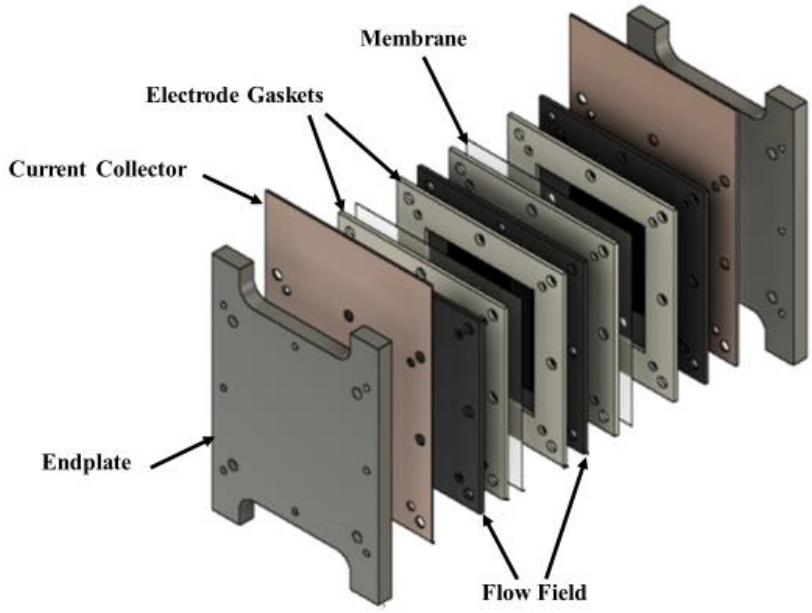


Figure 1. 4. A schematic of a simple VRFB cell assembly. All parts are tightened to each other by bolts and nuts.

Electrodes are electrically conductive and porous materials, which enable the electrolyte to trade electrons with external electrical circuit. The potential difference exerted on the system by the external circuit enforces the reaction direction in each electrolyte by obligating one side to give electrons and the other to take them. They are conventionally made out of graphite due to the high conductivity, stability, and corrosion resistance of this material. However, they possess poor electrochemical activity in vanadium redox reactions, which increases the overpotential required to charge and discharge VRFBs and hinders their energy efficiency and power density. [12–15] Numerous studies have recommended different electrode treatments, such as chemical, [12,15–22] thermal, [14,19,23] plasma [14] and electrochemical, [20,24] to improve the kinetics of the redox reaction. Moreover, Several studies have suggested using alternative cheap materials for electrodes. [25–29] A schematic of the flow field-electrode assembly is illustrated in Figure 1. 5.

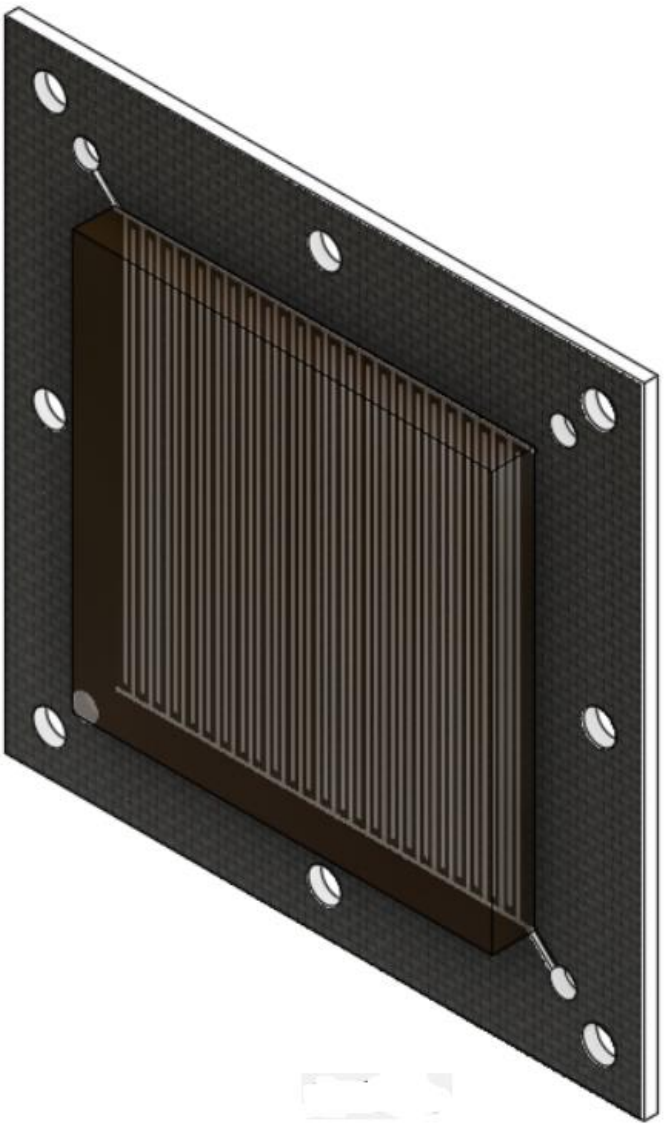

Figure 1. 5. A schematic of the flow field-electrode assembly. The electrode is compressed against the flow field and a fraction of the electrolyte, passing through the flow field channels, diffuses in the electrode.

The path taken by electrons passes electrodes, current collectors, and the external circuit, after electrochemical reactions take place in electrodes. A mutual ion must transfer between half-cells and trade electrons, to complete the reaction cycle of the electrochemical cell. Additionally, both negative and positive reactants must not move from one half-cell to the other. Therefore, the

presence of a membrane, enabling this selective ion crossover, is necessary between half-cells. These membranes are called IEMs. The most common IEMs are cation-exchange membranes (CEMs) and anion-exchange membranes (AEMs), which allow only protons and specific negative ions to cross-transfer, respectively. CEMs possess lower ionic resistances due to the higher mobility of protons. However, crossover of positive vanadium ions are frequent for typical acid and vanadium concentrations of VRFB electrolytes. AEMs do not permit the crossover of vanadium ions. However, their ionic conductivity is lower than CEMs, and their chemical stability has been proven to be unsatisfactory for an expected lifetime of 10~20 years. [30][31] Several research groups have developed modified CEMs, [32,33] amphoteric membranes [34] and bipolar membranes [35–37] to overcome the limitations of both AEMs and CEMs.

Flow field designs obligate electrolytes to flow through designed pathways. Several studies have reported that the presence of flow field plates reduces pump power and improves overall cell performance. [38–41] The most studied flow field designs are interdigitated flow fields (IFFs), serpentine flow fields (SFFs), and parallel flow fields (PFFs). These designs are shown in Figure 1. 6. IFFs and PFFs promise a lower pressure drop than SFF, however, the electrolytes flow is distributed unevenly in these FFs and the residence time of electrolytes in IFF and PFF is less in comparison to SSF for each reaction cycle. [42–46] It is debatable which FFs are superior at low current densities, however, it is evident that IFFs lose efficiency more rapidly than SFFs at high current densities due to ion transport limitations and presence of nearly stagnant zones due to non-uniform flow distribution. Therefore, the optimal flow field design depends on the parameters of the system for high current densities. [43,46–49]

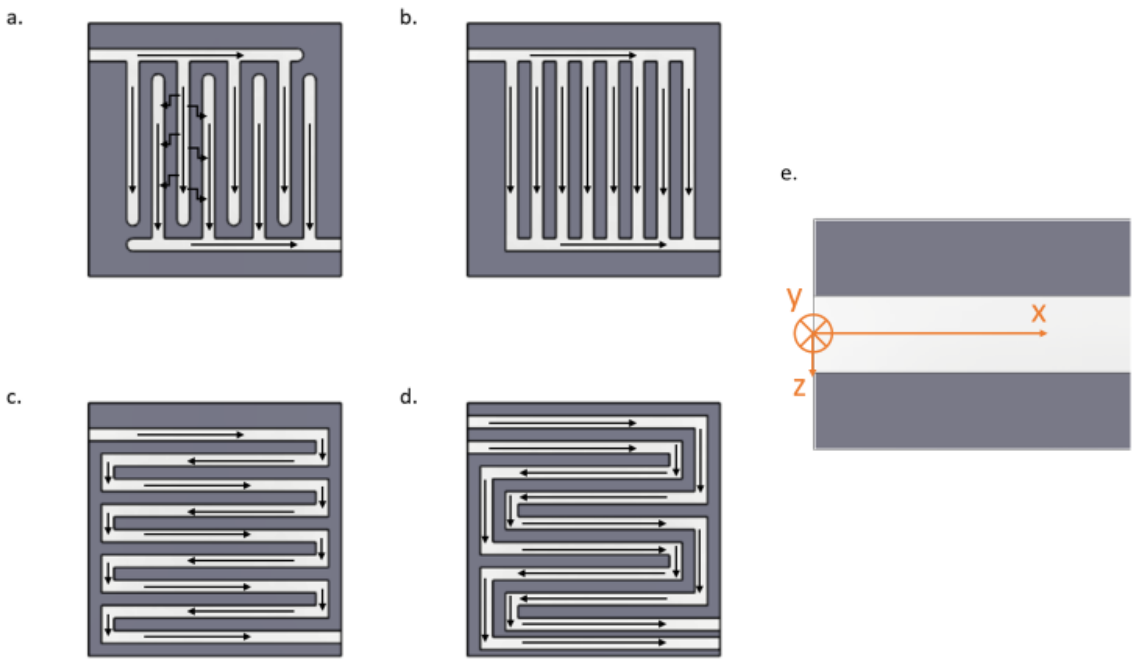


Figure 1. 6. Schematic of channels in a. IFF b. PFF c. single-channel serpentine (SSFF) and d. multi-channels serpentine flow field (MSFF) designs. Letter e represents a schematic of Cartesian coordinates directions in the channels.

## 1.3- Motivations of studying pressure distribution in RFBs

A key element affecting the performance of RFBs is the FF design. The pressure loss in RFB cells with IFF are generally less than the ones with SFF for the same active area, as mentioned in Section 1.3. However, electrolytes are maldistributed in RFB cells with IFF; therefore, the electrolyte (hence, the reactants) are unevenly exposed to the electrode, resulting in unbalanced current density distribution. [50] Numerous studies have mentioned that improving the uniformity of the current density distribution enhances the electrochemical performance of RFBs. [49–52] Therefore, since flow distribution is one of the parameters affecting current density distribution, this parameter is important to improving RFBs with IFF. Electrolyte pressure gradients dictate the

path of electrolytes in RFB cells. Hence, understanding the pressure distribution is necessary to control the flow maldistribution.

Moreover, the power demand of electrolytes pumps affects the efficiency of RFB systems. Several experimental studies have concluded that pumps are responsible for up to a 10% drop in the system efficiency of a large-scale VRFB. [53,54] Pump power consumption rate ($P_{pump}$) is directly linked to the overall pressure drop of electrolytes, as Equation 1.4 demonstrates: [55,56]

$$P_{pump} = \frac{Q\Delta P_{RFB}}{\eta_{pump}} \tag{1.4}$$

Where Q, $\Delta P_{RFB}$, and $\eta_{pump}$ are the electrolyte flow rate, the overall pressure drop of the RFB, and the pump efficiency, respectively. Larger pumps are less efficient, cost more, and consume greater power rate than smaller ones. [42,57,58] Equation 1.3 suggests that higher pump power is required for electrolyte flows with larger pressure drop. Previous studies have suggested that pumps cost 5-14% of the capital cost, [59,60] and 5-14% of the total cost of RFB systems. [61] The target total cost of energy storage systems is 100 $/KWh, and according to the studies, the total cost of pumps is at 50-120 $/KWh, exceeding the target limit at the most. Consequentially, reducing the cost and increasing the system efficiency of RFBs are motivations to study pressure distribution.

### 1.3.1- Literature review on modeling in RFBs and liquid-phase electrochemical devices

Numerous studies have suggested improvements to RFBs and liquid-phase electrochemical devices by modeling fluid dynamics. A summary of the studied phenomena and modeling approaches in literature are presented in Table 1. 1.

Although numerical approaches are more accurate than analytical ones, they are computationally more costly than analytical ones, and numerical modeling describes the system it was designed

for. therefore, it cannot predict correlations and trends between dependent and independent parameters in the system. Multiple parameter adjustments and recalculations are needed to do so, which results in more time-consuming measures. The flexibility of a model to parameter tuning is important to studying the target phenomena when stacking or scaling up the system. Therefore, the focus of this study is to use analytical approaches to model fluid dynamics and pressure distribution in RFBs.

A couple of studies have utilized analytical approaches to study fluid dynamics in RFB cells, as Table 1. 1 suggests. However, these studies lack sufficient explanations on fundamental fluid dynamics. Hence, analytical approaches require more investigation. In this study, a novel analytical model has been developed to model fluid dynamics in RFBs. Its accuracy is tested with experimental data and other similar models.

Table 1. 1. List of articles modeling fluid dynamics in RFBs or similar liquid-phase electrochemical devices.

| Reference | Studied Phenomena | Modeling approaches |
|---|---|---|
| [38] | The effect of geometrical parameters in IFFs on VRFB cell performance | 2-D coupled fluid dynamic, kinetics and mass transport simulation, 3-D CFD model, 1-D fluid dynamics model |
| [43] | The performance comparison between SSFF and IFF designs, flow and state of charge distribution in VRFB cells | Coupled 3-D CFD and mass transport model |

| Reference | Studied Phenomena | Modeling approaches |
|---|---|---|
| [49] | Effect of conventional FF, MSFF, and IFF geometry on flow distribution and performance of VRFB | Coupled 2-D CFD and analytical kinetics model |
| [55] | Pressure losses and flow rate optimization for a 40-cell VRFB stack | Analytical electrochemical and fluid dynamics modeling |
| [62] | Flow rate distribution, flow penetration to the electrode, and their effect on VRFBs with SFF performance | 3-D CFD coupled with analytical kinetics model |
| [63] | Hydrogen evolution in VRFBs | 2-D CFD and kinetics model |
| [64] | flow and current density distribution, and Zinc depositions in Zn-Br RFB | Coupled 2-D CFD, mass transport, and kinetics model |
| [65] | Performance of and temperature distribution in a kW-class VRFB stack | Coupled kinetics, mass transfer, and thermal model |
| [66] | Developing a model for current density distribution and transient state of charge in VRFBs with AEM | Coupled CFD, mass transport, and kinetics model |
| [67] | Ion transport through a porous separator in VRFB | Coupled transient 2-D CFD and mass transport model |
| [68] | Ion concentration and redox voltage distribution in VRFBs | Coupled 2-D CFD and mass transport model |

| Reference | Studied Phenomena | Modeling approaches |
|---|---|---|
| [69] | Velocity, ion concentration, overpotential, and current density distribution in VRFB cells | Coupled 3-D CFD, mass transport, and kinetics model |
| [70] | Effect of geometrical parameters on current density and overpotential distribution and cell performance in VRFBs | Coupled 3-D CFD and mass transport model |
| [71] | Effect of geometrical parameters on current density and overpotential distribution and cell performance in VRFBs with IFF | Coupled 3-D CFD and mass transport model |
| [72] | Flow rate distribution, flow penetration to the electrode, and their effect on VRFBs with SFF performance | Non-dimensionalized 3-D CFD coupled with analytical kinetics model |
| [73] | Concentration and overpotential distribution between cells in a multi-stack VRFB module, with performance modeling | Coupled CFD and mass transport model, considering transport delay in stacks |
| [74] | Residence time and velocity distribution in VRFBs with IFF | Coupled transient CFD and mass transport model |
| [75] | The effect of channel tapering on the pressure drop and flow distribution in RFBs with IFF | 2-D dimensionless CFD model |

| Reference | Studied Phenomena | Modeling approaches |
|---|---|---|
| [76] | Identifying heat sources, and the effect of electrolyte flow and current density distribution in the performance of VRFB stacks | Coupled 2-D CFD, mass transport, kinetics, and thermal model |
| [77] | Overpotential, ion concentration and current density distribution in VRFBs with IFF | Coupled 2-D CFD, mass transport, and kinetics model |
| [78] | Flow distribution in VRFBs with SFF, and velocity profile in the channels and electrode | 2-D CFD model |
| [79] | Pressure distribution in RFBs with Cerium as a reactant | CFD model with the turbulent flow approach |
| [80] | The role of the porous electrode on overpotential and current density distribution in VRFB cells | 3-D Lattice-Boltzmann model for fluid dynamics, coupled with mass transport and kinetics |
| [81] | The effect of flow rate, ions, and acid concentration on the performance of VRFBs during the discharge cycle | Coupled 2-D CFD, mass transport, and kinetics model |
| [82] | Flow distribution and pressure drop in VRFBs with PFF and IFF | 1-D analytical fluid dynamics model, 2-D CFD model |

| Reference | Studied Phenomena | Modeling approaches |
|---|---|---|
| [83] | Flow distribution and pressure drop in VRFBs with PFF, SFF, and IFF | 1-D analytical fluid dynamics model, 2-D, and 3-D CFD models |
| [84] | Operational modes for running a VRFB cell stack, and their effects on the stack's performance | Coupled analytical fluid dynamics, and mass transport model |
| [85] | The overall pressure drop, electrolyte flow distribution, and temperature in a VRFB cell stack | Coupled analytical fluid dynamics, thermal and mass transport model |
| [86] | Flow distribution and electrode flow rate proportion in VRFBs with SFF | Analytical fluid dynamics model |

## Chapter 2- Research objectives and approaches

The energy density of RFBs hinders the expansion of their large-scale applications. Flow maldistribution in RFBs is an important reason for non-uniform current density distribution, which affects the efficiency of RFB systems. Additionally, power consumption rate of electrolyte pumps is an energy sink. Therefore, the primary goal of this study is to develop an analytical approach to model the fluid dynamics in VRFB. It addresses the rarity of analytical knowledge to understand and improve the mentioned issues. Following objectives are defined to reach the overarching goal:

**Objective 1: Identifying a set of dimensionless numbers, important to experiment design for fluid dynamics in and scale-up of the RFBs.** A dimensional analysis is performed on the fluid dynamics of the RFB. A set of dimensionless numbers are identified numbers to design and control experiments. The effect of each number on the overall pressure drop of RFB cells is investigated.

**Objective 2: Modeling the electrolyte flow dynamics in RFB cells with IFF and SFF designs and identifying the key parameters.** Navier-Stokes and Darcy's are the governing equations to describe the system. A scaling analysis is performed on these equations to identify key parameters. A hydraulic-electrical analogous model is obtained from the scaling analysis to model the electrolyte flow dynamics.

**Objective 3: Identifying the key parameters affecting flow maldistribution in IFFs and suggesting improvements.** The hydraulic-electrical analogous model is utilized to predict the flow distribution in the parallel channels of IFF. Improvements to the flow distribution are proposed after the key parameters are identified by the model.

**Objective 4: Predicting the overall pressure drop for RFBs with IFF and SFF designs.** The overall pressure drop is predicted for RFBs. It is compared to experimental data to validate the model. The experimental data are achieved both from the literature and the designed experiments.

## Chapter 3- The analysis of fluid dynamics in the RFB

### 3.1- Introduction

#### 3.1.1- Navier-Stokes equations

Navier-Stokes (N-S) equations are a set of differential equations describing the motion of viscous fluids. They are stated as:

$$\begin{cases} \rho\left(\frac{\partial v_x}{\partial T} + (\overrightarrow{v_c}.\nabla)v_x\right) = -\rho g_x - \frac{\partial P_h}{\partial x} + \mu\nabla^2 v_x \\ \rho\left(\frac{\partial v_y}{\partial T} + (\overrightarrow{v_c}.\nabla)v_y\right) = -\rho g_y - \frac{\partial P_h}{\partial y} + \mu\nabla^2 v_y \\ \rho\left(\frac{\partial v_z}{\partial T} + (\overrightarrow{v_c}.\nabla)v_z\right) = -\rho g_z - \frac{\partial P_h}{\partial z} + \mu\nabla^2 v_z \end{cases} \quad (3.1)$$

Where ρ, v, $P_h$, μ, T, and g are the fluid density, velocity vector, hydraulic pressure, viscosity, time, and gravitational constant, respectively. The subscriptions x, y, and z represent the magnitude of the assignee vector mirrored on these Cartesian axes. The first term on the left-hand side (LHS) of each N-S equation accounts for the transient pressure effect, as the second term represents the impact of inertial forces. The first term on the right-hand side (RHS) expresses gravitational forces effect, the second term embodies the hydraulic pressure effect, and the last one accounts for the impact of viscous forces.

N-S equations may be represented in fewer terms than their depictions in Equation 3.1. gravitational forces and hydraulic pressure terms are combined to form a term called modified pressure ($P_m$). Modified pressure is defined as: [87]

$$P_m = P_h + \rho g h \quad (3.2)$$

gravitational forces are path-independent and only the flow elevation effects their magnitude. Therefore, the modified pressure gradient is obtained as:

$$\nabla P_m = \nabla P_h + \nabla \rho g h = \nabla P_h + \rho g \nabla h = \nabla P_h + \rho g \tag{3.3}$$

Now, N-S equations can be reiterated in fewer terms:

$$\begin{cases} \rho\left(\frac{\partial v_x}{\partial T} + (\overrightarrow{v_c}.\nabla)v_x\right) = -\frac{\partial P_m}{\partial x} + \mu\nabla^2 v_x \\ \rho\left(\frac{\partial v_y}{\partial T} + (\overrightarrow{v_c}.\nabla)v_y\right) = -\frac{\partial P_m}{\partial y} + \mu\nabla^2 v_y \\ \rho\left(\frac{\partial v_z}{\partial T} + (\overrightarrow{v_c}.\nabla)v_z\right) = -\frac{\partial P_m}{\partial z} + \mu\nabla^2 v_z \end{cases} \tag{3.4}$$

Moving forward, the modified pressure is called pressure in the body of thesis. Other definitions of pressure will be mentioned if needed.

### 3.1.2- Darcy's law for porous media

The fluid dynamics in porous media is dominated by viscous forces at relatively low flow rates. Darcy's experimental law is an established equation to predict the pressure gradient for laminar flow passing through porous media:

$$\nabla P_m = -\frac{\mu}{K}\vec{v} \tag{3.5}$$

Where K is an experimental term called the permeability of porous media. Darcy's law predicts the dominancy of viscous forces. Additionally, it shows the pressure gradient depends on the flow average velocity, viscosity, and permeability. However, when the fluid flow rate increases, microscopic inertial forces grow rapidly. Therefore, the pressure gradient deviates from what Darcy's law predicts. Many experimental terms are suggested to account for this deviation. [88] The most well-known ones are Forchheimer and Brinkman correction terms in the literature.

Forchheimer presented a general correction term to Darcy's law for fluids at high flow rates in his article at 1901: [89]

$$\nabla P_m = -\frac{\mu}{K} v_p - \beta \rho v_p^2 \tag{3.6}$$

Where β is a coefficient. Numerous studies have investigated the mechanism behind the Forchheimer term. The latest narrative on what is this mechanism is that the Forchheimer term represents the microscopic form drag force due to the presence of solid obstacles. [89–92] Ruth and Ma have the same opinion on what Forchheimer term represents, however, they challenge the uniqueness of this solution and present complicated solutions. Moreover, they present a similar dimensionless number to Reynolds number, which considers both the amount of flow rate and the geometric structure of the porous medium, to evaluate the necessity of Forchheimer term. However, the classic form of Forchheimer term is still used in the literature due to its simplicity and accuracy. [38,43,79]

Several studies suggested equations to calculate β. [90,92] However, Joseph's and Nield's modification to Darcy's law is an established one: [38,93]

$$\nabla P_m = -\frac{\mu}{K} v_p - \frac{C_F}{\sqrt{K}} \rho |v_p| v_p \tag{3.6a}$$

Where $C_F$ is the Forchheimer coefficient. The maximum value of the Forchheimer coefficient is 0.55, however, it can be less than 0.55 if the diameter of solid particles in porous media is in order of one-tenth of the hydraulic diameter of porous media. [88] In this study, the Forchheimer coefficient is assumed to be 0.55 due to the high porosity of the electrodes in the RFB systems.

Another facet that Darcy's law overlooks is the viscous shear stress of the fluid that opposes the flow. Brinkman introduced a term, adapted from steady state N-S equations, to account for the above-mentioned effect: [94]

$$\nabla P_m = -\frac{\mu}{K} v_p + \acute{\mu} \nabla^2 v_p \tag{3.7}$$

Where μ´ is the effective viscosity. Brinkman assumed the inertial terms are negligible, therefore, he only considered the viscous terms in N-S equations. He chose to use the fluid viscosity instead of the effective viscosity after refuting other available options. However, later studies have stated that the effective viscosity depends both on the fluid viscosity and the system geometry. [90,95] Uncertainties and rarity of knowledge on the relationship between geometry and effective viscosity obligates studies to use the fluid viscosity as the effective viscosity in Brinkmann correction term. [38,43,79] Here, it is assumed to be the same. Therefore, the corrected Darcy's law is represented as:

$$\nabla P_m = -\frac{\mu}{K} v_p - \frac{0.55}{\sqrt{K}} \rho |v_p| v_p + \mu \nabla^2 v_p \tag{3.8}$$

The necessity of using the modified version for this study is investigated in Section 3.4.

### 3.1.3- Dimensional analysis

Buckingham pi theorem is an analytical tool developed by E. Buckingham, which describes important parameters of the studied system in terms of dimensionless numbers (DN). These DNs provide a basis for experiment design. Empirical equations may be developed by using these numbers. Dimensional analysis is often used for scaling up or data analysis. [87,96–98]

Based on the Buckingham pi theorem, the number of DNs, which describe the system, is the number of the variables subtracted by the number of independent units. For example, Mukherjee, B. et. al. [97] found that nine parameters affect oil droplet size generated during chemical dispersion of crude oil, and the involved independent units are mass, length, and time. Therefore, six DNs are sufficient to describe the system and control the experiments with.

### 3.1.4- Scaling analysis

Scaling analysis predicts the order of magnitude for involved parameters in modeling. [87,98] For example, Equation 3.9 is extracted from the fluid continuity equation in a long channel by utilizing scaling analysis:

$$\nabla v = 0 \rightarrow \frac{\partial v_x}{\partial x} + \frac{\partial v_y}{\partial y} + \frac{\partial v_z}{\partial z} = 0, \frac{\partial v_x}{\partial x} = O\left(\frac{v_x}{L}\right), \frac{\partial v_y}{\partial y} = O\left(\frac{v_y}{w}\right), \frac{\partial v_z}{\partial z} = O\left(\frac{v_z}{h}\right)$$

$$\xrightarrow{scaling} \frac{v_x}{L} + \frac{v_y}{w} + \frac{v_z}{h} = 0,\ t, h \ll L \rightarrow v_y, v_z \ll v_x \tag{3.9}$$

Where L, w, and h are the channel's length, width, and height, respectively. The performed scaling analysis suggests that the fluid velocity magnitude in the x-direction is greater than the same in y- and z-directions. By the same rationale, the velocity in y- and z-direction is neglected for further analysis in this document.

### 3.1.5- Studied flow field designs

The analyses, models, and experiments in this study are implemented on IFFs, SSFFs, and 3-channel serpentine flow fields (3SFFs). Figure 1. 6 demonstrates schematic of these flow fields. IFFs forces the electrolytes to pass through the electrode by making them jump over FF ribs, which ensures full contact between the electrolyte flow and electrodes. However, as Wang et. al. suggested, the residence time in IFFs is lower than SFFs, which results in lower reaction extent in each cycle. [99] Moreover, as mentioned in Chapter 1, it is expected for RFB cells with SFF to have higher pressure loss than the ones with IFF.

## 3.2- Dimensional analysis of fluid dynamics in VRFB

Based on Buckingham pi theorem, the number of DNs describing the system is the number of variables subtracted by the number of independent units.

$$\Delta P_m = f\left(w_r, K, \mu, v_c, L, \rho, h_c, w_c, h_p\right), mass, time\ and\ length\ are\ units$$

$$\rightarrow number\ of\ dimensionless\ numbers = 9 - 3 = 6$$

Where $w_r$, $w_c$, $v_c$, L, and $h_c$ are the width of ribs, width of channels, velocity in channels, length of channels, and height of channels, respectively. Finding dimensionless numbers requires a set of recurring variables. Each variable must provide a dimensionless number when integrated with this set of recurring variables. To ensure this condition, the criteria for choosing recurring variables are:

1- Each of the independent units must appear in at least one of the variables.
2- Forming a dimensionless group out of variables within the recurring set must not be possible.

$\rho$, $v_c$, and $h_c$ are the chosen set of recurring variables. Each variable forms a dimensionless number by manipulating the recurring variables. MATLAB RREF function is a tool that assists forming dimensionless numbers out of the set of recurring variables and the target variable. It implements Gauss-Jordan elimination method on its input matrix to return a reduced row echelon form (RREF) of the matrix. Each row in the input matrix represents an assigned independent unit, and each column represents a variable and its dimensions. The RREF function transforms this matrix into an output matrix, which each variable are compared to the recurring variables instead of the independent units. The recurring variables must occupy the first columns.

| | $\rho$ | $v_c$ | $h_c$ | $\Delta P_m$ | $\mu$ | K | L | $w_c$ | $h_p$ |
|---|---|---|---|---|---|---|---|---|---|
| Mass | 1 | 0 | 0 | 1 | 1 | 0 | 0 | 0 | 0 |
| Length | -3 | 1 | 1 | -1 | -1 | 2 | 1 | 1 | 1 |
| Time | 0 | -1 | 0 | -2 | -1 | 0 | 0 | 0 | 0 |

After implementing RREF function:

| | ρ | $v_c$ | $h_c$ | $\Delta P_m$ | μ | K | L | $w_c$ | $h_c$ |
|---|---|---|---|---|---|---|---|---|---|
| ρ | 1 | 0 | 0 | 1 | 1 | 0 | 0 | 0 | 0 |
| $v_c$ | 0 | 1 | 0 | 2 | 1 | 0 | 0 | 0 | 0 |
| $h_p$ | 0 | 0 | 1 | 0 | 1 | 2 | 1 | 1 | 1 |

$$Eu = f\left(Re, \frac{K}{h_p^2}, \frac{w_r}{h_p}, \frac{w_c}{h_p}, \frac{h_c}{h_p}, \frac{L}{h_p}\right), Eu = \frac{\Delta P_m}{\rho v_c^2}, Re = \frac{\rho v_c h_c}{\mu}$$

$$\rightarrow Eu = \acute{A}\, Re^a\, \tilde{K}^b\, \widetilde{w_r}^c\, \widetilde{w_c}^d\, \tilde{L}^e\, \widetilde{h_c}^d \tag{3.10}$$

Where Eu and Re are the Euler number and the Reynolds number, respectively. A representation of $\tilde{K}$ is by using a DN called compression ratio (CR):

$$CR = 1 - \frac{h_p}{h_{p,0}} \tag{3.11}$$

Which $h_{p,0}$ is the uncompressed electrode thickness. Based on the literature, the permeability and the thickness of porous media has a linear correlation with each other.[38,100] This correlation leads to the following equations:

$$K = K_0 \frac{h_p}{h_{p,0}} = K_0(1 - CR) \tag{3.12}$$

$$\widetilde{K} = \frac{K}{h_p^2} = \frac{K_0(1-CR)}{\left(h_{p,0}(1-CR)\right)^2} = \frac{K_0}{h_{p,0}^2} \frac{1}{1-CR} \tag{3.13}$$

Which $K_0$ is the uncompressed permeability. This representation of $\tilde{K}$ shows the linear relationship between the permeability and the thickness of electrodes, and a single parameter (CR) substitutes

two parameters ($h_p$ and K) for tuning $\tilde{K}$. Therefore, it is easier to use for designing and controlling experiments or predicting the behavior of the system while scaling up.

3.3- Assumptions for further analysis of the fluid dynamics in the RFBs

i. RFB systems are in steady state. The charging and discharging cycles for RFBs usually take hours, and they reach a steady state in a couple of minutes. Therefore, this assumption is a strong one for simplification of the modeling process.

ii. The flow is laminar. Based on the literature, the maximum Reynolds number for the laminar flow in a round pipe is around 2100. Reynolds numbers between 2100 to 4000 signifies a transitional flow, and flows with Reynolds numbers beyond 4000 are turbulent. [101] It is a strong assumption for the RFB cells with IFF due to possessing numerous parallel channels in their designs, but it can be a weak one for SSFF and MSFF, where the electrolyte flow passes through one channel and a couple of parallel channels, respectively.

iii. The entrance region in channels is negligible. In the entrance region, boundary layer, which viscous forces are dominant, is not fully developed. For a laminar flow, the length of the entrance region is predicted as:

$$\frac{l_e}{D} = 0.06Re \tag{3.14}$$

The strength of this assumption is investigated in Section 3.2.2.

iv. The flow velocity vector direction is in the direction of the length of channels (x-direction) and the velocity gradient direction is in the direction of the thickness and height of channels (z- and y-direction, respectively). The strength of this assumption is supported by employing scaling analysis on the fluid continuity equation, as done in Section 3.1.4.

v. The pressure gradient in lateral directions is negligible. The strength of this assumption is supported by implementing scaling analysis on N-S equations, as done in Section 3.3.1.

3.3.1- Scaling analysis on N-S equations

$$\begin{cases} \rho\left(\frac{\partial v_x}{\partial t} + (v_c.\nabla)v_x\right) = -\frac{\partial P_m}{\partial x} + \mu\nabla^2 v_x \\ \rho\left(\frac{\partial v_y}{\partial t} + (v_c.\nabla)v_y\right) = -\frac{\partial P_m}{\partial y} + \mu\nabla^2 v_y \xrightarrow{Steady\ State} \\ \rho\left(\frac{\partial v_z}{\partial t} + (v_c.\nabla)v_z\right) = -\frac{\partial P_m}{\partial z} + \mu\nabla^2 v_z \end{cases}$$

$$\begin{cases} \rho\left(v_x\frac{\partial v_x}{\partial x} + v_y\frac{\partial v_x}{\partial y} + v_z\frac{\partial v_x}{\partial z}\right) = \frac{\partial P_m}{\partial x} + \mu\left(\frac{\partial^2 v_x}{\partial x^2} + \frac{\partial^2 v_x}{\partial y^2} + \frac{\partial^2 v_x}{\partial z^2}\right) \\ \rho\left(v_x\frac{\partial v_y}{\partial x} + v_y\frac{\partial v_y}{\partial y} + v_z\frac{\partial v_y}{\partial z}\right) = -\frac{\partial P_m}{\partial y} + \mu\left(\frac{\partial^2 v_y}{\partial x^2} + \frac{\partial^2 v_y}{\partial y^2} + \frac{\partial^2 v_y}{\partial z^2}\right) \\ \rho\left(v_x\frac{\partial v_z}{\partial x} + v_y\frac{\partial v_z}{\partial y} + v_z\frac{\partial v_z}{\partial z}\right) = -\frac{\partial P_m}{\partial z} + \mu\left(\frac{\partial^2 v_z}{\partial x^2} + \frac{\partial^2 v_z}{\partial y^2} + \frac{\partial^2 v_z}{\partial z^2}\right) \end{cases}$$

The second and third rows contain six terms containing negligible $v_y$ and $v_z$ and two terms of pressure gradients in y- and z-direction, respectively. Equating these negligible terms to their respective pressure gradients results in them being negligible too. Therefore, the first row suffices for modeling the system:

$$\rho\left(v_x\frac{\partial v_x}{\partial x}\right) = -\frac{dP_m}{dx} + \mu\left(\frac{\partial^2 v_x}{\partial x^2} + \frac{\partial^2 v_x}{\partial y^2} + \frac{\partial^2 v_x}{\partial z^2}\right)$$

$$\frac{dP_m}{dx} = \mu\frac{d^2 v_c}{dy^2} + \mu\frac{d^2 v_c}{dz^2} + \mu\frac{d^2 v_c}{dx^2} - \rho v_c\frac{dv_c}{dx} \tag{3.15}$$

Macroscopic mass conservation equation for RFBs demonstrates that the velocity vector magnitude for the efflux and influx is equal:

$$\dot{m}_{in} = \dot{m}_{out} \xrightarrow{\rho=cte} (vA)_{in} = (vA)_{out} \xrightarrow{A_{in}=A_{out}} v_{in} = v_{out}$$

This equation applies the entire flow passage. Therefore, it is assumed that the velocity gradient in the x-direction equals zero. This conclusion leads to:

$$\frac{dP_m}{dx} = \mu \frac{d^2 v_c}{dy^2} + \mu \frac{d^2 v_c}{dz^2} \tag{3.16}$$

This equation is used for further analysis in channels of FFs.

### 3.3.2- Entrance region length

To validate the assumption about the negligibility of the entrance region in FFs, the entrance region length is calculated through Equation 3.14 for the RFB cells in the lab within their working range. As demonstrated in Figure 3. 1, the maximum entrance region length for each FF design is around 3% of their respective channels' length, (overall channel's length for each FF design is mentioned in Section 3.7). Hence, neglecting the entrance region is a strong assumption for further analysis.

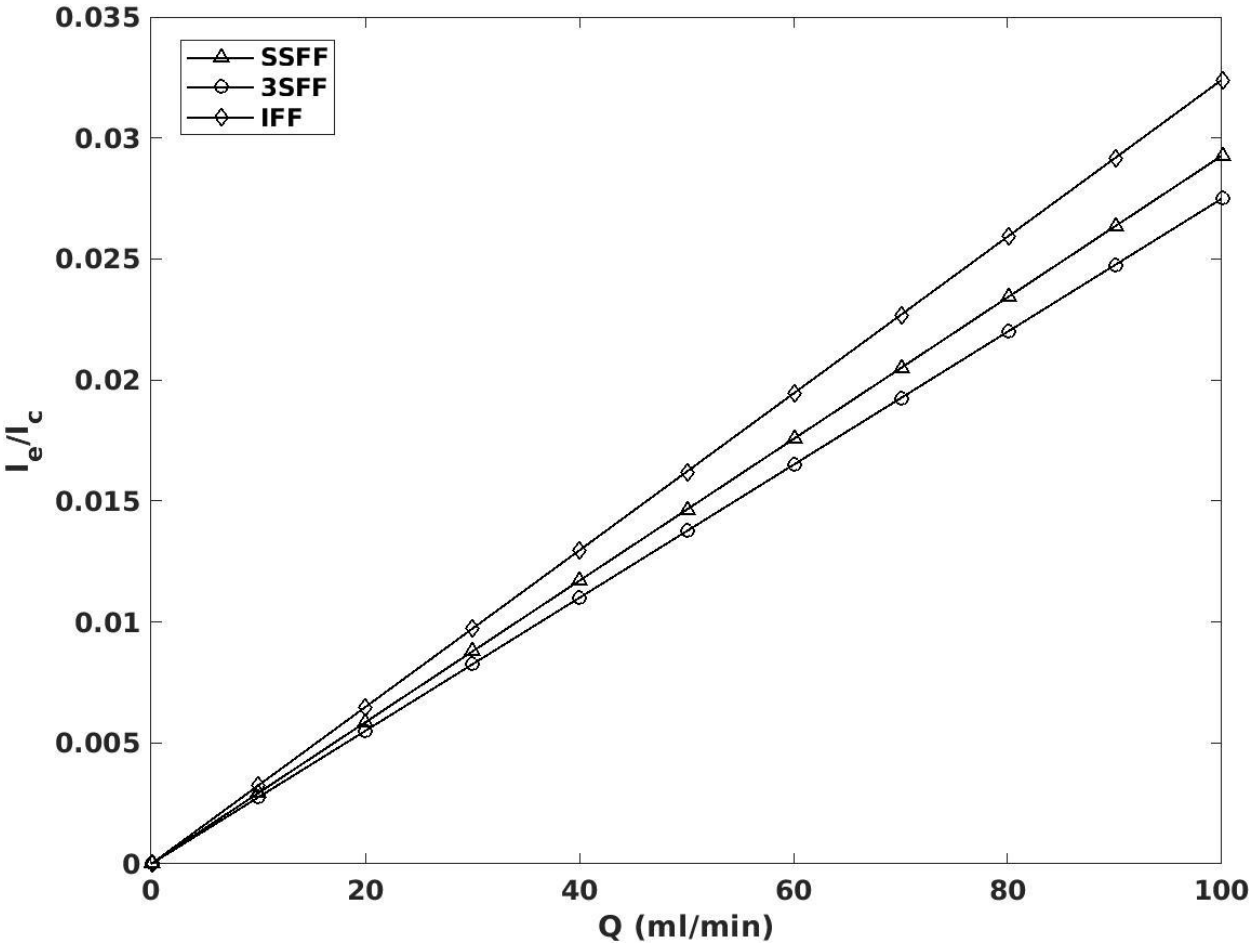


Figure 3. 1. The entrance region length for different vanadium electrolyte flow rates in single-channel serpentine (SSFF), 3-channels serpentine (3SFF), and interdigitated (IFF) flow fields with 25cm$^2$ active area.

## 3.4- Scaling analysis of the fluid dynamics in VRFB

### 3.4.1- Analysis of the fluid dynamics in the non-porous medium

The governing equation for the fluid dynamics in the non-porous medium is:

$$\frac{dP_m}{dx} = \mu \frac{d^2 v_c}{dy^2} + \mu \frac{d^2 v_c}{dz^2} \tag{3.17}$$

By implementing a scaling analysis, Equation 3.18 is produced:

$$\frac{\Delta P_m}{L} = \mu \frac{v_c}{{h_c}^2} + \mu \frac{v_c}{{w_c}^2} \rightarrow \Delta P_m = O\left(L\left(\mu \frac{v_c}{{h_c}^2} + \mu \frac{v_c}{{w_c}^2}\right)\right) \tag{3.18}$$

A DN is formed by dividing the first term over the second one to find the dominant term on the RHS:

$$\frac{\mu \frac{v_c}{{h_c}^2}}{\mu \frac{v_c}{{w_c}^2}} = \frac{{w_c}^2}{{h_c}^2} = \widetilde{w}_c,\ \widetilde{w}_c = \frac{Viscous\ Forces\ in\ y-direction}{Viscous\ Forces\ in\ z-direction} \tag{3.19}$$

$\tilde{w}_c$ is in order of 1 for the most cases studied, therefore, both terms are considered for further analysis. The governing equation is reiterated as:

$$\frac{dP_m}{dx} = \mu \frac{d^2 v_c}{dy^2} + \mu \frac{d^2 v_c}{dz^2} \tag{3.20}$$

3.4.2- Analysis of the fluid dynamics in the porous medium

The governing equation for the fluid dynamics in the porous medium is:

$$\frac{dP_m}{dx} = \frac{\mu}{K} v_p + \frac{0.55}{\sqrt{K}} \rho |v_p| v_p + \mu \frac{\partial^2 v_p}{\partial x^2} + \mu \frac{\partial^2 v_p}{\partial y^2} + \mu \frac{\partial^2 v_p}{\partial y^2} \tag{3.21}$$

By implementing a scaling analysis, Equation 3.22 is produced:

$$\frac{\Delta P_m}{L} = \frac{\mu}{K} v_p + \frac{0.55}{\sqrt{K}} \rho {v_p}^2 + \mu \frac{v_p}{{h_p}^2} + \mu \frac{v_p}{{t_p}^2} + \mu \frac{v_p}{{l_p}^2} \tag{3.22}$$

DNs are formed by dividing each term over the others to find the dominant terms on the RHS:

$$\begin{cases} DN1 = \dfrac{\mu \frac{v_p}{{h_p}^2}}{\frac{\mu}{K} v_p} = \dfrac{K}{h_p^2} = \dfrac{Brinkmann\ in\ y-direction}{Darcy's\ law} \\ DN2 = \dfrac{\mu \frac{v_p}{{t_p}^2}}{\frac{\mu}{K} v_p} = \dfrac{K}{t_p^2} = \dfrac{Brinkmann\ \ in\ x-direction}{Darcy's\ law} \\ DN3 = \dfrac{\mu \frac{v_p}{{l_p}^2}}{\frac{\mu}{K} v_p} = \dfrac{K}{l_p^2} = \dfrac{Brinkmann\ \ in\ z-direction}{Darcy's\ law} \end{cases} \tag{3.23}$$

$$DN4 = \frac{\frac{\mu}{K}v_p}{\frac{0.55}{\sqrt{K}}\rho {v_p}^2} = \frac{\mu}{0.55 v_p \rho \sqrt{K}} = \frac{Darcy's\ Law}{Forchheimer} \tag{3.24}$$

Where DN1, DN2, DN3, DN4 are arbitrary dimensionless numbers. DN1, DN2, and DN3 do not depend on flow rate and are in the order of $10^{-4}$~$10^{-6}$ for the usual RFBs. These orders of magnitude justifies neglecting the Brinkman terms. As Figure 3. 2 demonstrates, DN4 is in the order of 100 at the least, which points out the dominancy of Darcy's law over Forchheimer term. Therefore, Darcy's law suffices for describing the pressure gradient in the porous medium:

$$\frac{dP_m}{dx} = \frac{\mu}{K} v_p \tag{3.25}$$

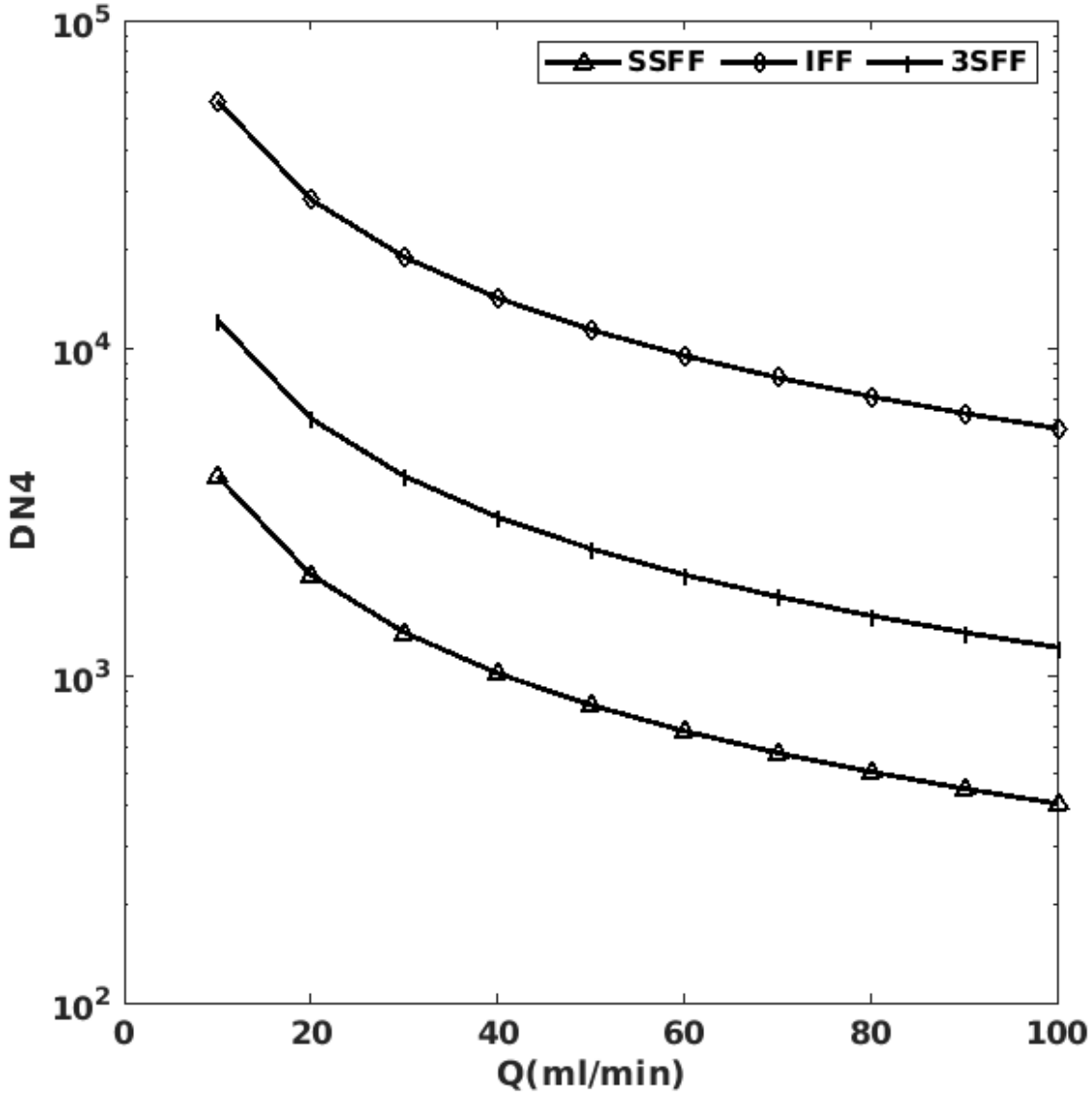


Figure 3. 2. DN4 for different flow rates of the electrolytes for single-channel serpentine (SSFF), 3-channel serpentine (3SFF), and interdigitated (IFF) flow field designs.

3.4.3- Flow rate proportion in the porous and non-porous media of the flow field

As stated in Assumption v, the pressure at the interface of porous and non-porous media is a continuous entity. Therefore, the magnitude of pressure gradients in both media must be in the same order, too:

$$\frac{\Delta P_m}{L} = \mu\left(\frac{\bar{v_c}}{w_c^2} + \frac{\bar{v_c}}{h_c^2}\right) = A_1\frac{-\mu\overline{v_p}}{K}, A_1 = a\ constant\ in\ the\ order\ of\ 1$$

By applying the properties of the RFBs in the lab, Equation 3.26 is reached:

$$Q_c = \acute{A}_1 Q_p \times 10^3, Q\ in \frac{ml}{s}, \acute{A}_1 = O(1) \tag{3.26}$$

Equation 3.26 demonstrates that more than 99% of the flow in the channel passes the non-porous medium, and less than 1% diffuse in the porous medium above the channels. This result justifies the following assumption that the amount of flow passing the electrode above the channels is negligible. The fundamentals of the hydraulic-electrical analogous model are based on this assumption. However, the model is modified further to relax the error of this assumption.

3.5- Hydraulic-electrical analogous model (HEAM)

HEAM is developed by assuming the electrode above the channels acts like an impermeable wall justified by the small amount of flow diffusing in the electrode. Moreover, it is assumed that the entrance region is negligible, therefore, viscous forces are the only dominant forces in the channels. For Round pipes, the Hagen-Poiseuille profile is obtained by applying the Newton's second law of motion: [101]

$$v(r) = \left(\frac{\Delta P_m D^2}{16\mu l}\right)\left[1 - (\frac{2r}{D})^2\right] \tag{3.27}$$

Where r, $v_{(r)}$, D, μ, and l are the distance of an arbitrary point from the centerline of the pipe, fluid velocity at radius r, pipe diameter, fluid dynamic viscosity, and pipe length, respectively. Poiseuille's Law is achieved by integrating this velocity profile over the cross-sectional area:

$$Q = \frac{\pi D^4 \Delta p}{128 \mu l} \tag{3.28}$$

Where Q is the fluid flow rate. A similar relationship between the fluid flow rate and the pressure drop is obtained by applying a dimensional analysis on the fluid dynamics in the system:

$$Q = f(D, l, \mu, \Delta P_m) \rightarrow \frac{\pi D^3 \Delta P}{4 \mu Q} = C \frac{l}{D} \rightarrow Q = \frac{\pi D^4}{4 C \mu l} \Delta P_m \tag{3.29}$$

Where C is a constant based on the geometry of the cross-sectional area of the pipe. By comparing Equations 3.28 and 3.29, it is concluded that C-value is 32 for round pipes. Some C-values for square pipes are mentioned in Equation 3.30: [101]

$$\begin{cases} C = 31.1, \ if \ \frac{a}{b} = 0.5 \\ C = 29, if \ \frac{a}{b} = 0.75 \\ C = 28.5, \ if \ \frac{a}{b} = 1 \end{cases} \tag{3.30}$$

Where a and b are the height and width of the pipe, respectively. The pipe hydraulic diameter ($D_h = \frac{2ab}{a+b}$) replaces the pipe diameter in Equation 3.29 for a square pipe. However, the actual velocity profile differs from what is described here, and portions of the flow diffuse in the electrode. Therefore, the actual pressure drop is lower than the one predicted by Poiseuille's law. To accommodate for the deviation from the pipe assumption, the C-value in Equation 3.29 is adjusted to a value between zero and C-values for pipes, mentioned in Equation 3.30. This value is fitted to the data for each FF and electrode design to enhance the accuracy of the HEAM. The

C-value is the only parameter fitted to the data; other parameters are obtained from FF or electrolyte properties of studied RFBs.

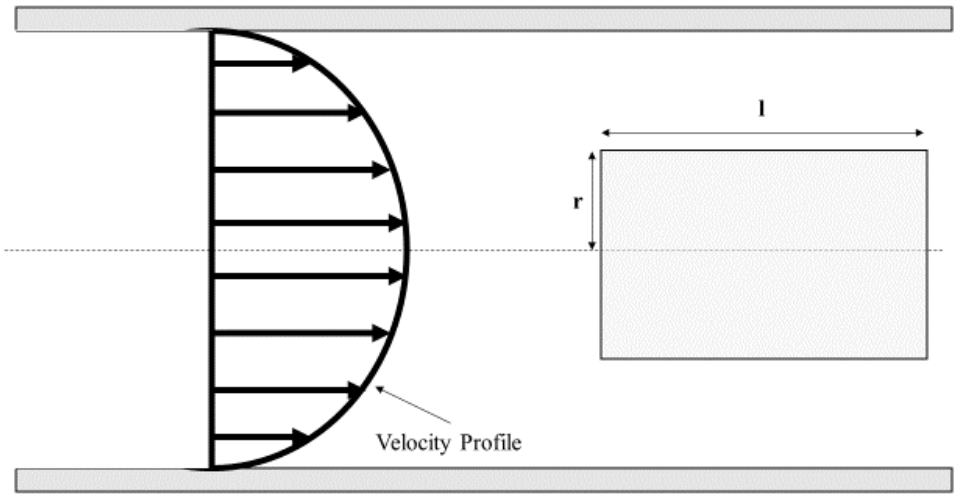


Figure 3. 3. A schematic of the pipe assumption and the flow velocity profile for round pipes in laminar, fully developed viscous flow.

Equation 3.29 is sufficient to relate the pressure drop and flow rate in SFF designs. However, an additional equation is required to link the pressure drop and flow rate in the obligatory path through the electrode above the ribs in IFF designs. Darcy's law is the governing equation for the flow passing through the electrode and is reiterated as:

$$\frac{\Delta P}{w_r} = \frac{\mu}{k}\frac{Q}{h_p l_r} \rightarrow \Delta P_m = \frac{\mu}{k}\frac{Q w_r}{h_p l_r} \tag{3.31}$$

Where $w_r$, $l_r$, $h_p$, and k are the width of the ribs, length of the ribs, electrode height, and electrode permeability, respectively. Figure 3. 4 schematically represents the geometric parameters in IFF designs.

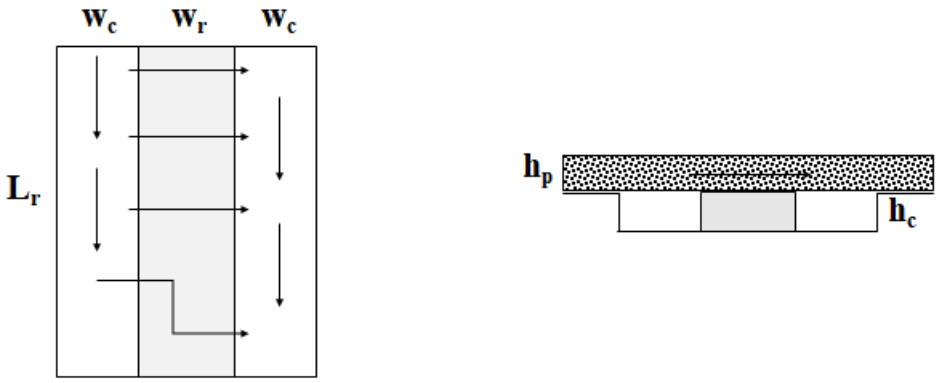


Figure 3. 4. A Schematic of the geometry and the flow directions for channels in IFF, from the top and front view. The left white, right white, and grey area represent inlet channels, outlet channels, and rib between inlet and outlet channels, respectively.

As Figure 1. 5 shows, Channels in IFF and SFF designs are not straight and bend many times to ensure electrolytes exposure to the electrodes. These bends cause pressure loss due to forcing fluid momentum change. These losses are called minor losses. Minor losses are stated in terms of equivalent length. Equivalent length of a minor loss is defined as the length of pipe of the same size as the minor loss, that would cause the same pressure drop as the minor loss. Table 3. 1 presents the equivalent length for minor losses in IFF and SFF designs. Length of channels is corrected by the equivalent length of each bend for pressure loss calculation in HEAM.

Table 3. 1. The equivalent length for minor losses present in IFF and SFF [102]

| Minor losses | Equivalent length ($L_{eq}/d_h$) |
|---|---|
| 180˚ return bend | 50 |
| 90˚ standard elbow | 30 |

To model the flow in FFs, it is assumed that the flow rate is analogous to the electrical current and the pressure is analogous to the electrical potential due to their same behavior in series or parallel channels or electrical circuits. In electrical circuits, the relationship between electrical current and potential is expressed as:

$$V = R_{el} I$$

where V, I, and $R_e$ are electrical potential, current, and resistance, respectively. The same relationship may be written for Q and ΔP as well:

$$\Delta P_m = R_v Q \tag{3.32}$$

where $R_v$ is the viscous resistance for the respective porous or non-porous medium. The viscous resistances for the channels and porous medium can be obtained by manipulating Equations 3.29 and 3.31:

$$Q = \frac{\pi {D_h}^4}{4C\mu l} \Delta P_m \rightarrow R_c = \frac{4C\mu l}{\pi {D_h}^4} \tag{3.33}$$

$$\frac{\Delta P_m}{w_r} = \frac{\mu}{k} \frac{Q}{h_p l_r} \rightarrow R_p = \frac{\mu w_r}{k h_p l_r} \tag{3.34}$$

Kirchhoff's laws quantify how current flows through and how potential varies in an electrical circuit. They are described as the following statements:

1- In each node, the sum of the current is zero (ΣI=0).

2- In each loop, the sum of the potential is zero (ΣV=0).

   2a- The potential difference between two nodes is equal to the resistance between them multiplied by the passing current. ($V_{ij}= R_{ij}I_{ij}$)

2b- The potential difference is negative while moving co-current and is positive while moving counter-current.

Figure 3. 5 demonstrates a representation of the HEAM for a 5-channels IFF and a 3SFF. A set of linear equations is formed by using this representation and Kirchhoff's laws. The potential of every node and the current between each is found by solving the described system of linear equations. Through these analyses, Objective 2 is accomplished.

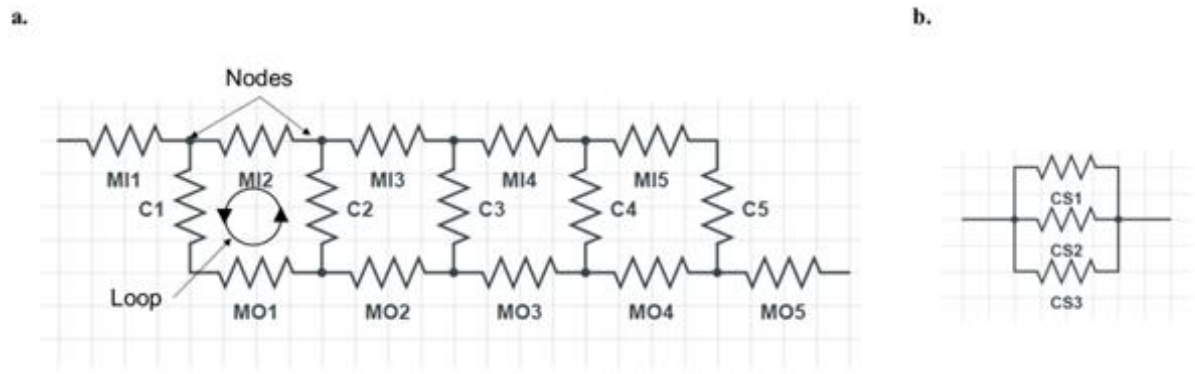


Figure 3. 5. A HEAM representation for a. 5-channel IFF b. 3-channel SFF (3SFF). Abbreviation used in figure are: MI: the inlet manifold resistance, C: a set of inlet, rib and outlet channel resistance, MO: the outlet manifold resistance, CS: a parallel channel in SFF

## 3.6- Similar models in the literature

Two similar models were developed for only PFF and IFF designs in the literature. Both studies establish a set of equations to predict mean velocity and pressure drop in PFF. Subsequently, these parameters are converted to the ones in IFF by utilizing an equation from Darling and Perry's research. [103] summarizes their final formulae. In this study, the accuracy of HEAM is compared to the accuracy of both models.

Table 3. 2. The pressure drop formulae for PFF and IFF from the literature.

| Reference | PFF set of equations | IFF set of equations |
|---|---|---|
| Gerhardt, Wong, Aziz [38] | $\Delta P_{PFF} = \frac{64\mu Q L_c (w_c + w_r)}{w_{FF} w_c h_c d_h^2}$ | |
| MacDonald, Darling [82,83] | $\Delta P_{PFF} = \frac{32\mu v_p L_c}{\psi d_h^2}$<br>$\psi = 1.5 - 2.0330a + 2.9201a^2 - 2.5518a^3 + 1.4366a^4 - 0.3806a^5$<br>$a = \min(h_c, w_c)/\max(h_c, w_c)$<br>$v_c = \frac{Q}{N A_c}$<br>$\begin{cases} PFF: v_p = \frac{32 v_c K^2}{A_c} \\ IFF: v_p = \frac{Q}{N h_p L_c} \end{cases}$ | $\Delta P_{IFF} = \Delta P_{PFF}\left(1 + \frac{2 + 2\cosh\beta}{\beta \sinh\beta}\right)$<br>$\beta^2 = \frac{128 L_c^2 K h_p}{w_r w_c h_c d_h^2}$ |

## 3.7- Experimental setup

### 3.7.1- Differential pressure measurement assembly (DPMA)

As illustrated in Figure 3. 6, the DPMA consists of a differential pressure gauge (DPG) (Dwyer Capsuhelic differential pressure gauge- series 4000), tubing, and connectors. T-connectors draw portions of the flow from inlet and outlet of the RFB cell and are guided to the DPG. The Capsuhelic DPG measures the pressure difference by a fixed-ended silicone rubber diaphragm, which its center is connected to a precision spring. The high-pressure fluid line is connected to the front of the diaphragm, while the low-pressure one is connected to the back. The difference in the applied pressure by both lines deforms the diaphragm, which its displacement at the center is reported by the gauge indicator attached to the precision spring (A side cross-sectional diagram of

the Capsuhelic assembly is presented on [104]). This displacement has a linear relationship with the applied pressure difference, as the pressure distribution is uniform on the diaphragm. [105]

U-shaped tubes are placed before the DPG to host vacuum pump oil between the acidic solution and metal compartments of the DPG due to their low chemical tolerance to sulfuric acid. Vacuum pump oil is metal-compatible and immiscible at atmospheric pressures with sulfuric acid. However, the pressure at the high-pressure line allows sulfuric acid diffusion in the vacuum pump oil and forces sulfuric acid leakage into the DPG. Additionally, it forces some portion of the vacuum oil to be forcibly mixed with the electrolytes. Therefore, recharging the vacuum oil is necessary after a couple of experiments.

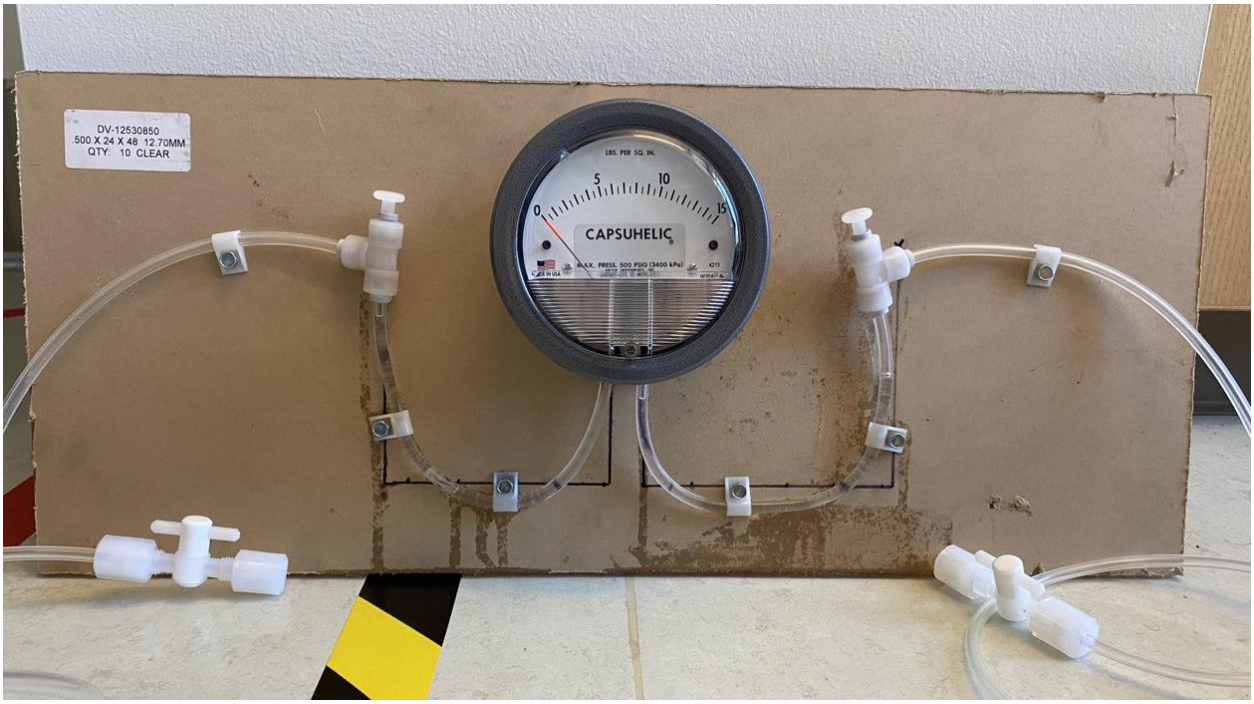


Figure 3. 6. DPMA system.

The acid leakage in DPG corrodes the diaphragm, introducing systematic errors. Silicone rubber is resistant to sulfuric acid; however, the diaphragm support is composed of steel, susceptible to

sulfuric acid. This corrosion changes the position of the center of the diaphragm, introducing zero error to the system, as the captured data in Figure 3. *7* illustrates. However, it should not affect the slope between the reported pressure drop and the flow rate due to the precision spring not being exposed to the acid and the linear relationship between the diaphragm center displacement and the applied pressure remaining the same.

The pressure drop of RFB cells is zero if the flow rate is zero. Hence, the regression line of data in graphs presenting the relationship between the pressure drop and the flow rate must pass the origin of the graph. Therefore, an approach to omit the zero error is to shift the captured data by the y-interception of the regression line, ensuring that the regression line passes the origin of the pressure drop-flow rate graph for each set of experiments.

### 3.7.2- Sources of errors in measurements

The absence of fluctuations and zero-error due to the misplacement of the indicator in the pressure and flow rate measurements was evident. The flow rate and the pressure were measured by the Masterflex L/S- precision tubing pump and the Capsuhelic DPG, with the accuracy of 0.08 ml/min and 3%, respectively.

### 3.7.3- The RFB cell

The properties of flow fields, electrolytes, and electrodes in the RFB cell is presented in Table 3. 3. Sigracell GFD4.6EA carbon felt and Sigracell 39-AA carbon paper are utilized as electrodes. Further information about flow fields and electrolytes in Aziz's and Messaggi's experiments are available in their respective articles. [38,43]

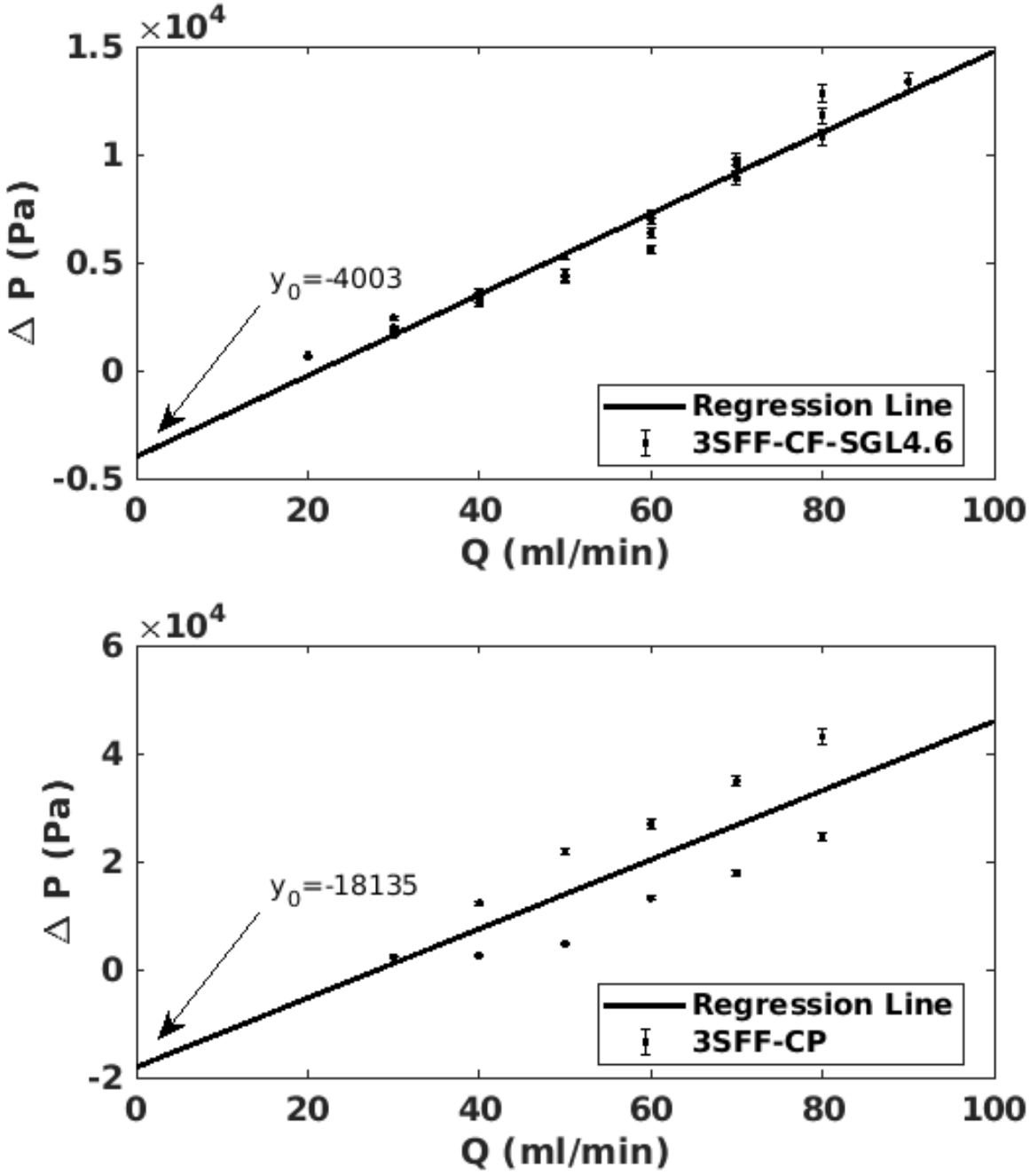


Figure 3. 7. Pressure drop- flow rate data and their respective regression lines for two different experimental settings. The zero error of each is shown on each subfigure.

Table 3. 3. The properties of flow fields, electrolytes, and electrodes in the RFB cell

| | Parameter | Value | Reference |
|---|---|---|---|
| RFB | Active area | 25 $cm^2$ | |
| FF | Width of ribs | 1 mm | |
| | Hydraulic diameter of channels | 1 mm | |
| IFF | Length of channels | 4.6 cm | |
| | Length of Manifold | 5 cm | |
| SSFF | Length of channels | 155 cm | |
| | Number of 180˚ return bends | 15 | |
| 3SFF | Length of channels | 55 cm | |
| | Number of 180˚ return bends | 5 | |
| Electrolytes | $VOSO_4$ concentration | 1 M | |
| | $H_2SO_4$ concentration | 3 M | |
| | Viscosity | 3.02 mPa.s | |
| | Density | 1270 $kg/m^3$ | |
| Electrode felt | Nominal thickness | 4.6 mm | |
| | Compressed thickness | 4 mm | |
| | Permeability (for 24% CR) | 65~68 $(\mu m)^2$ | [100] |
| | Permeability (for 0% CR) | 85~90 $(\mu m)^2$ | |
| Electrode paper | Nominal thickness | 280 µm | |
| | Compressed thickness | 230 µm | |
| | Permeability | ~17.5 $(\mu m)^2$ | [38,43] |

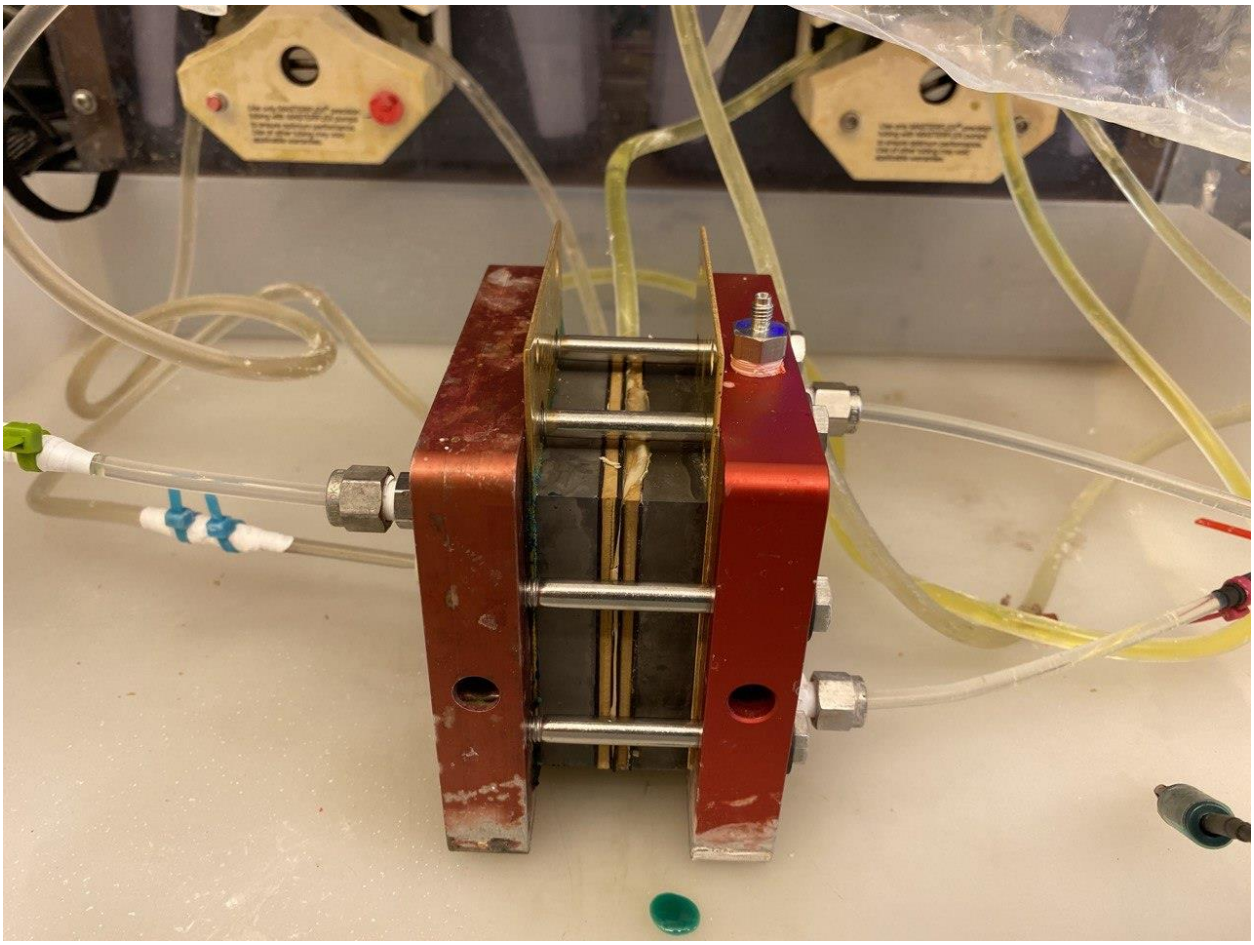

Figure 3. 8. 25 $cm^2$ RFB assembly.

## 3.8- Results and discussions

### 3.8.1- Investigating the accuracy of the HEAM

HEAM needs to prove its accuracy to be utilized for further analysis. Therefore, its accuracy is tested by comparing it to the corrected data from designed experiments and the data from the literature, as illustrated in Figure 3. 9-13. HEAM is sufficiently accurate at predicting pressure drop for RFBs with SFF design (<25% error), however, it is inconsistent to predict the same for RFBs with IFF design (Up to 200% error). This inconsistency roots in the modeling of electrodes, as there are no fitting parameter to relax the error of the model. However, the HEAM accuracy is

comparable to CFD models in the literature, showing that it is as reliable as computationally-costly CFD models at predicting fluid dynamics in RFBs. This result shows the promise of the HEAM model to be utilized as a cost-effective tool to predict pressure drop and improved with further research. Table 3. 4 provides a list of C-values used in each HEAM generated for Figure 3. 9-13.

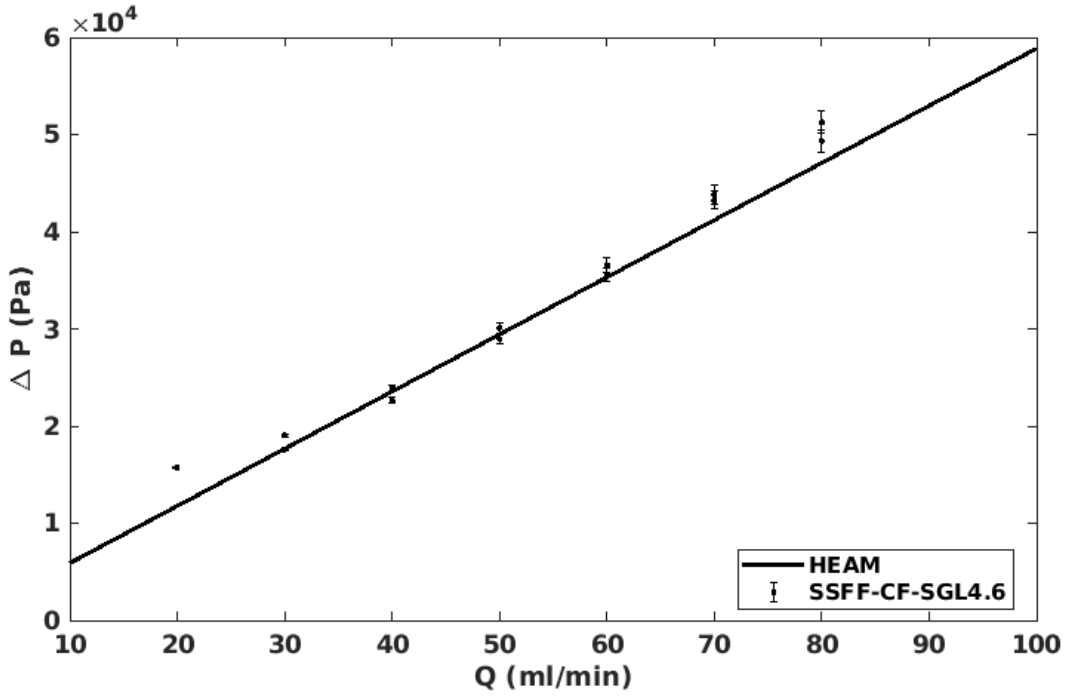


Figure 3. 9. Experimental and predicted pressure drop by HEAM for different electrolyte flow rates. The data are produced by designed experiments in the lab, and are shifted by the zero error to ensure the effects of systematic errors are removed. (CF: Carbon felt, SGL 4.6: 4.6 mm thick electrode)

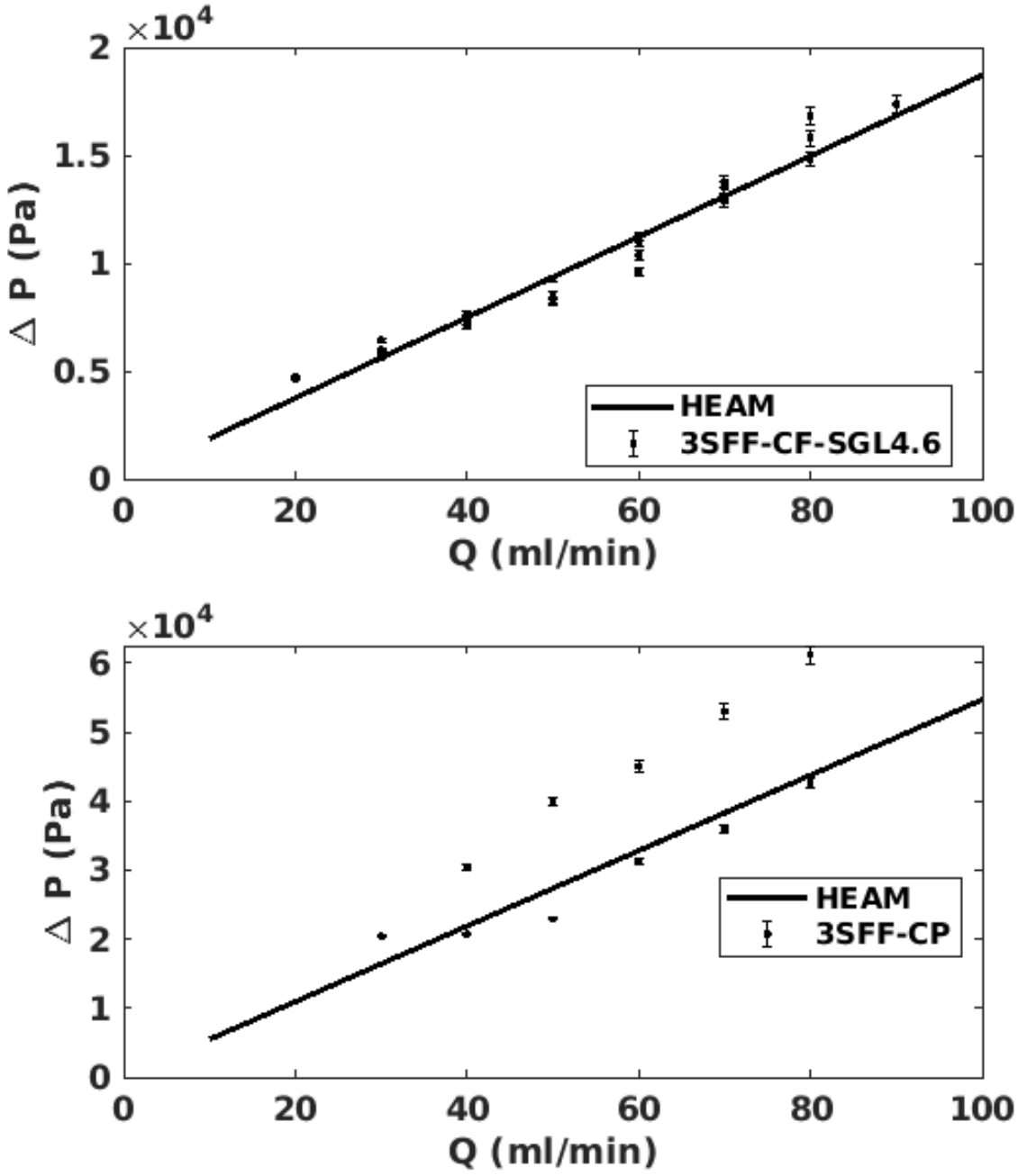


Figure 3. 10. Experimental and predicted pressure drop by HEAM for different electrolyte flow rates. The data are produced by designed experiments in the lab, and are shifted by the zero error to ensure the effects of systematic errors are removed. (CP: Carbon paper, CF: Carbon felt, SGL 4.6: 4.6 mm thick electrode)

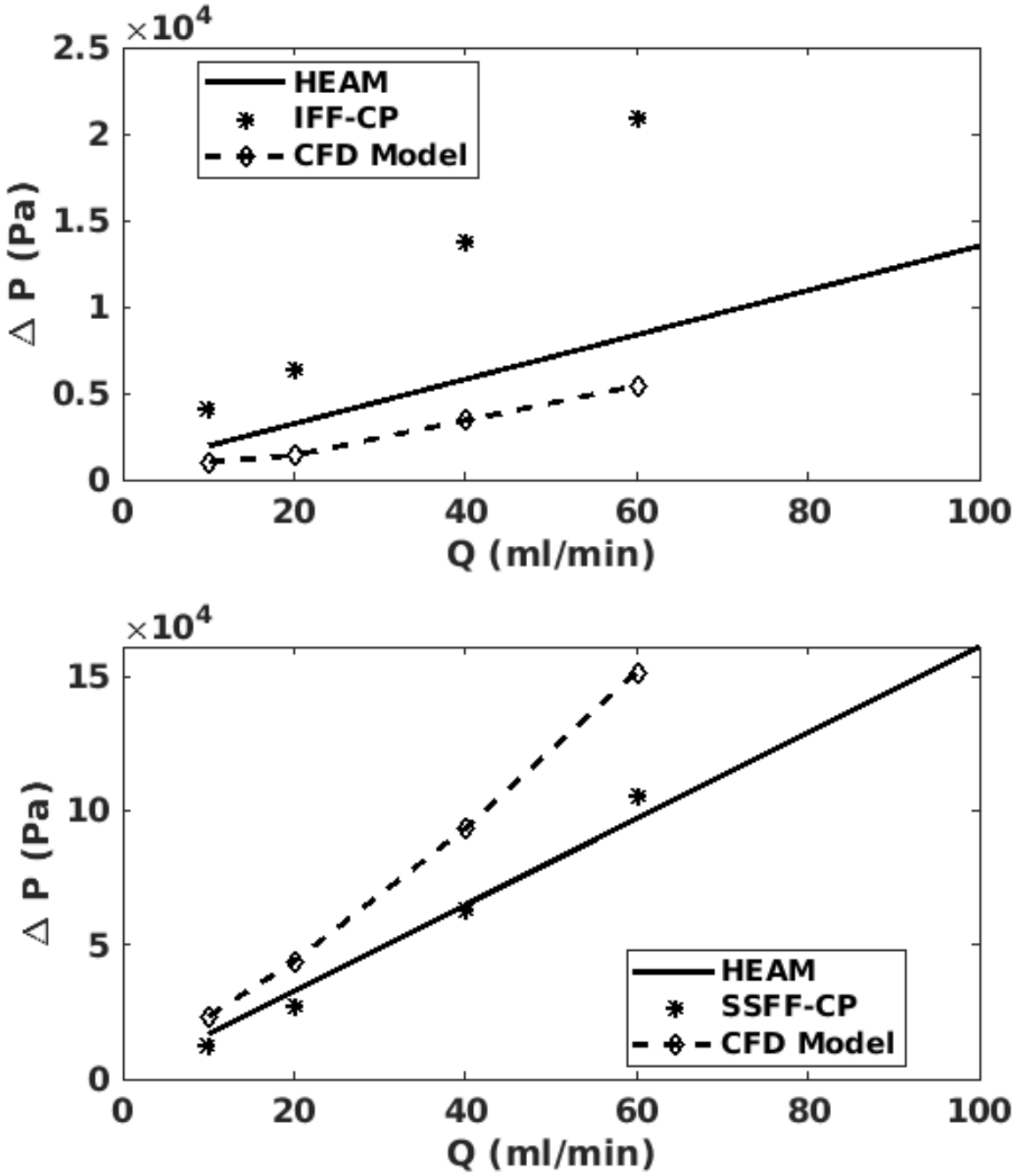


Figure 3. 11. Experimental and predicted pressure drop by HEAM and CFD models for different electrolyte flow rates. The data are for flow fields from the Messaggi's article. [43] (CFD: Computational fluid dynamics, CP: Carbon paper)

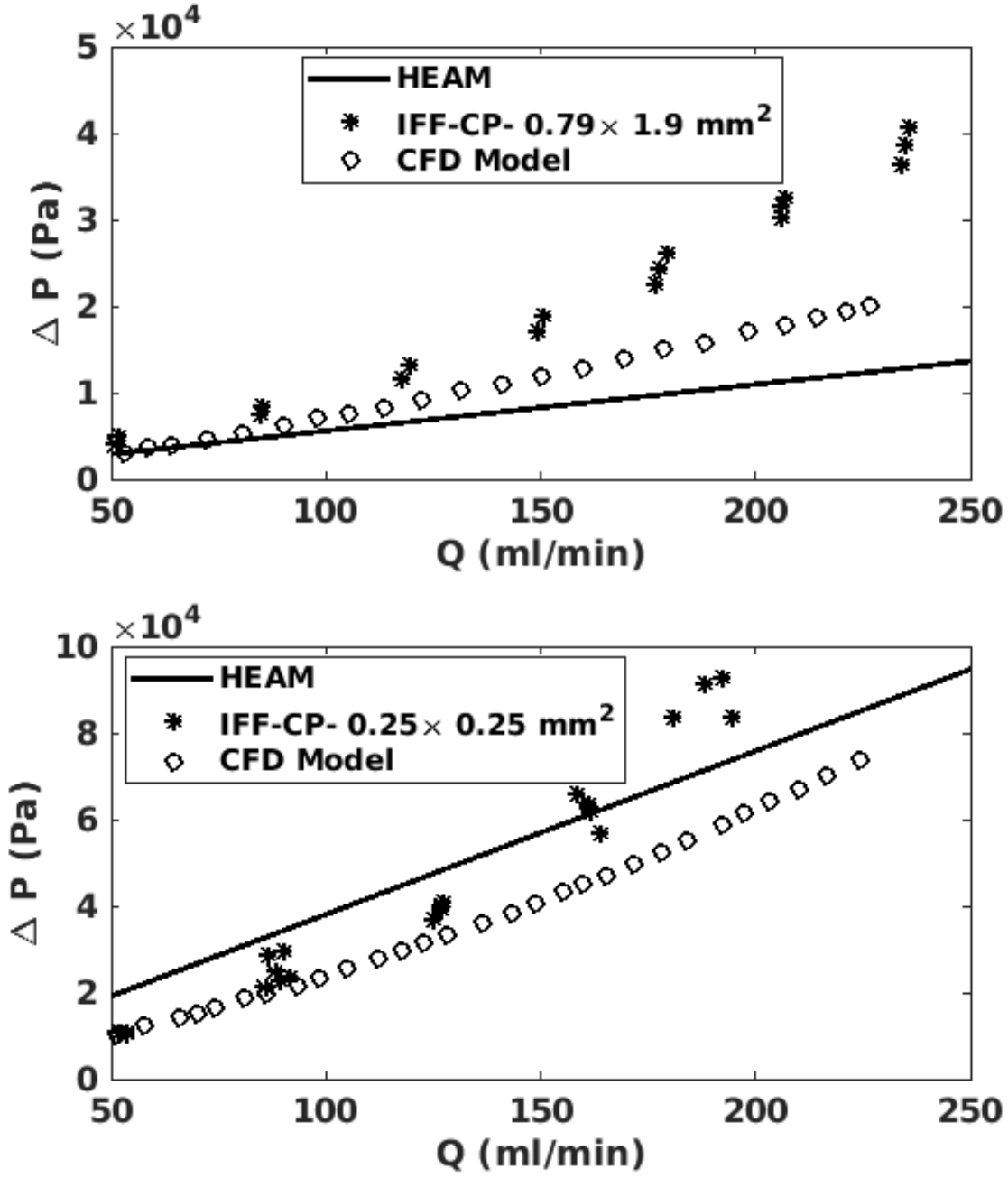


Figure 3. 12. Experimental, and predicted pressure drop by HEAM and CFD models for different electrolyte flow rates. The data are for an IFF flow field with the channel size of 1.59 mm × 1.9 mm from the Aziz's article. [38] (CFD: Computational fluid dynamics, CP: Carbon paper)

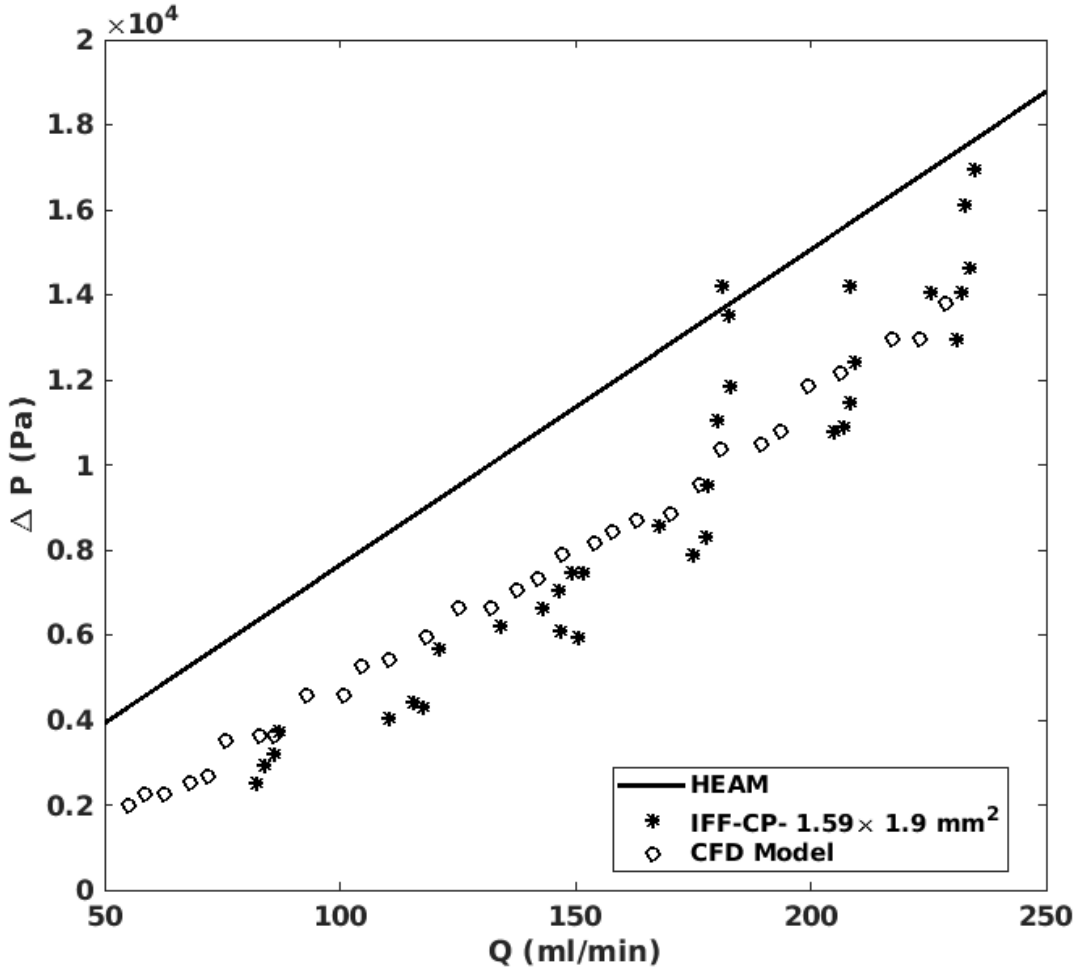


Figure 3. 13. Experimental, and predicted pressure drop by HEAM and CFD models for different electrolyte flow rates. The data are for a VRFB with IFF with the channel size of 1.59 mm × 1.9 mm from the Aziz's article. [38] (CFD: Computational fluid dynamics, CP: Carbon paper)

Table 3. 4. C-values for each data.

| Reference- flow field- electrode | C |
|---|---|
| SSFF- SGL 4.6 carbon felt | 6 |
| 3SFF- SGL 4.6 carbon felt | 12 |
| 3SFF- Carbon paper | 32 |
| [43]- IFF- Carbon paper | 32 |
| [43]- SSFF- Carbon paper | 6 |
| [38]- IFF-1.59w- Carbon paper | 0 |
| [38]- IFF-0.79w- Carbon paper | 7 |
| [38]- IFF-0.25w- Carbon paper | 32 |

Additionally, it is important to evaluate whether the HEAM is more accurate than its competitive analytical models in the literature or not. As Figure 3. 17-14 suggest, the HEAM is more accurate than MacDonald's and Aziz's analytical model. Additionally, as Figure 3. 16-16 suggest, it predicts that the pressure drop decreases as the cross-sectional area of channels becomes larger, which the other two models predict the opposite. Equation 3.35 shows how MacDonald's model falsely predicts that the pressure drop increases with the cross-sectional area of channels for RFBs with IFF design. The same is shown for Aziz's model in Equation 3.36.

$$\beta \to 0 \Rightarrow \begin{cases} \cosh\beta \to 1 \\ \sinh\beta \to \beta \end{cases} \Rightarrow \left(1 + \frac{2 + 2\cosh\beta}{\beta \sinh\beta}\right) \to 1 + \frac{4}{\beta^2} \xrightarrow{\frac{4}{\beta^2} > 1} \frac{4}{\beta^2} \Rightarrow \Delta P_{IFF} \to \Delta P_{PFF}\left(\frac{4}{\beta^2}\right)$$

$$\begin{cases} \Delta P_{PFF} = \frac{32\mu v_p L_c}{\psi d_h^2} \\ \beta^2 = \frac{128 L_c^2 K h_p}{w_r w_c h_c d_h^2} \end{cases} \Rightarrow \Delta P_{IFF} \to \frac{w_r w_c h_c \mu v_p}{\psi L_c h_p K} = \frac{w_r \mu Q}{\psi {L_c}^2 {h_p}^2 K} \frac{A_c}{N} \tag{3.35}$$

$$\beta \to 0 \Rightarrow \begin{cases} \cosh\beta \to 1 \\ \sinh\beta \to \beta \end{cases} \Rightarrow \left(1 + \frac{2 + 2\cosh\beta}{\beta \sinh\beta}\right) \to 1 + \frac{4}{\beta^2} \xrightarrow{\frac{4}{\beta^2} > 1} \frac{4}{\beta^2} \Rightarrow \Delta P_{IFF} \to \Delta P_{PFF}\left(\frac{4}{\beta^2}\right)$$

$$\begin{cases} \Delta P_{PFF} = \frac{64\mu Q L_c (w_c + w_r)}{w_{FF} w_c h_c d_h^2} \\ \beta^2 = \frac{128 L_c^2 K h_p}{w_r w_c h_c d_h^2} \end{cases} \Rightarrow \Delta P_{IFF} \to \frac{\mu Q (w_c + w_r) w_r}{2 L_c K h_p w_{FF}} = \frac{w_r \mu Q}{2 L_c K h_p w_{FF}} (w_c + w_r) \qquad (3.36)$$

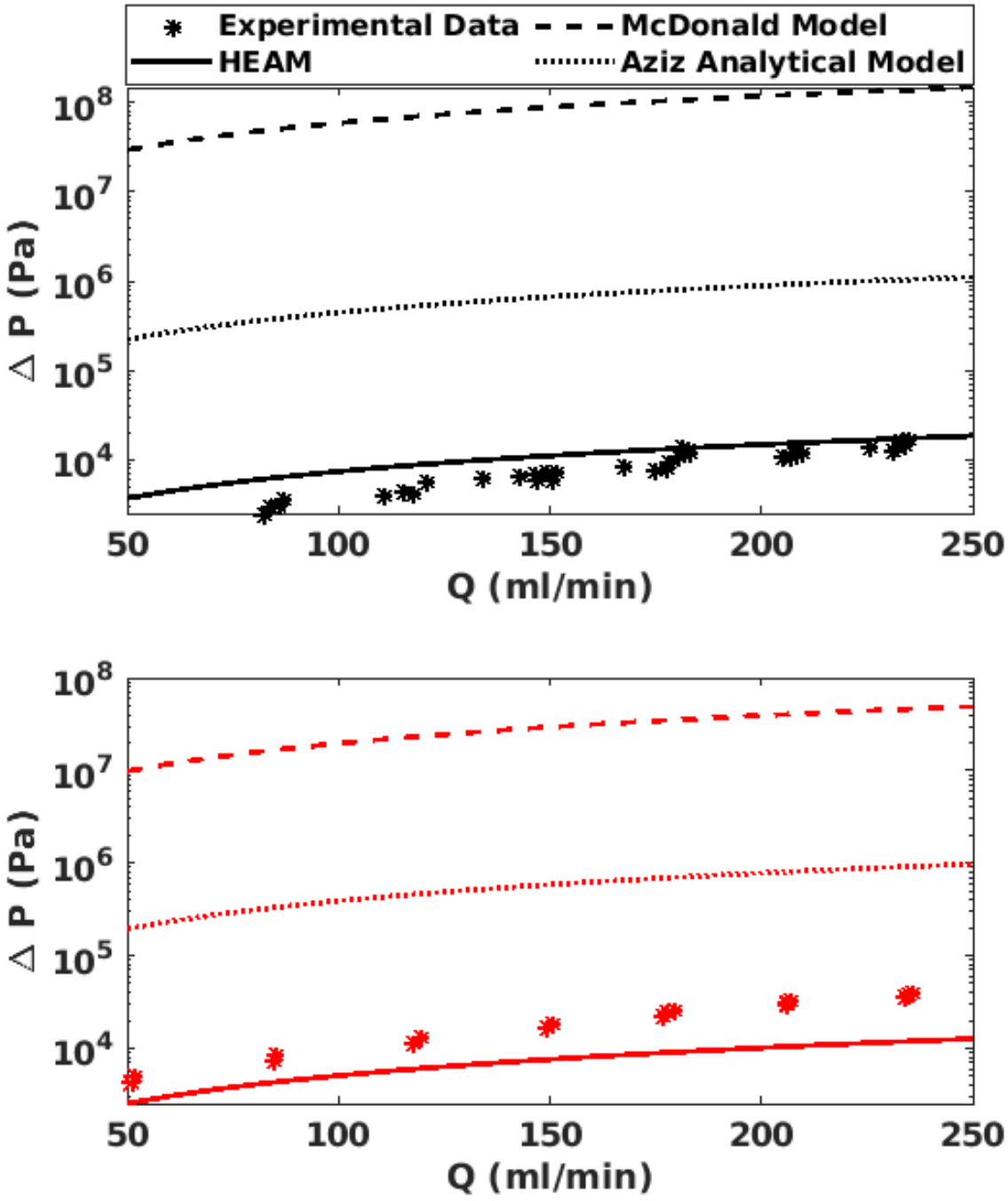


Figure 3. 14. Experimental and predicted pressure drop for IFFs with different channel dimensions by different models. (Red: 0.79 mm× 1.9 mm- 6 parallel channels, Black: 1.59 mm× 1.9 mm- 4 parallel channels) HEAM is more accurate than Aziz and MacDonald's models at predicting the pressure drop in both cases.

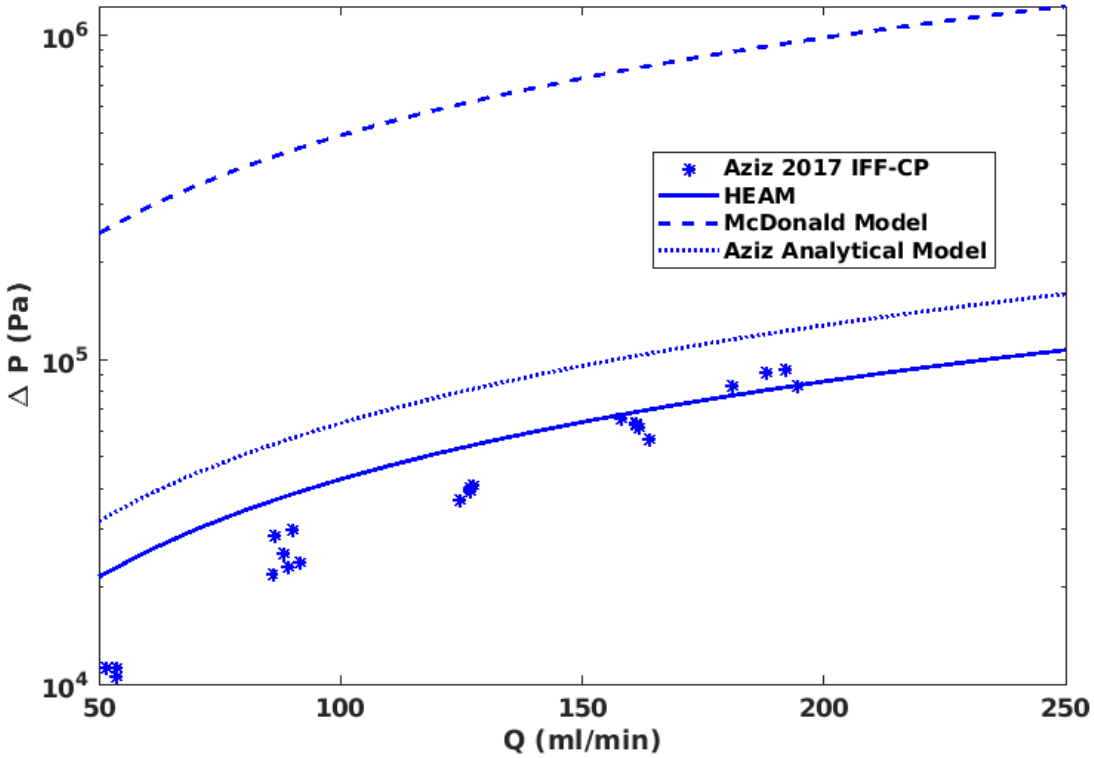


Figure 3. 15. Experimental and predicted pressure drop for IFFs with different channel dimensions by different models. (Blue: 0.25 mm× 0.25 mm- 10 parallel channels) HEAM is more accurate than Aziz and MacDonald's models at predicting the pressure drop.

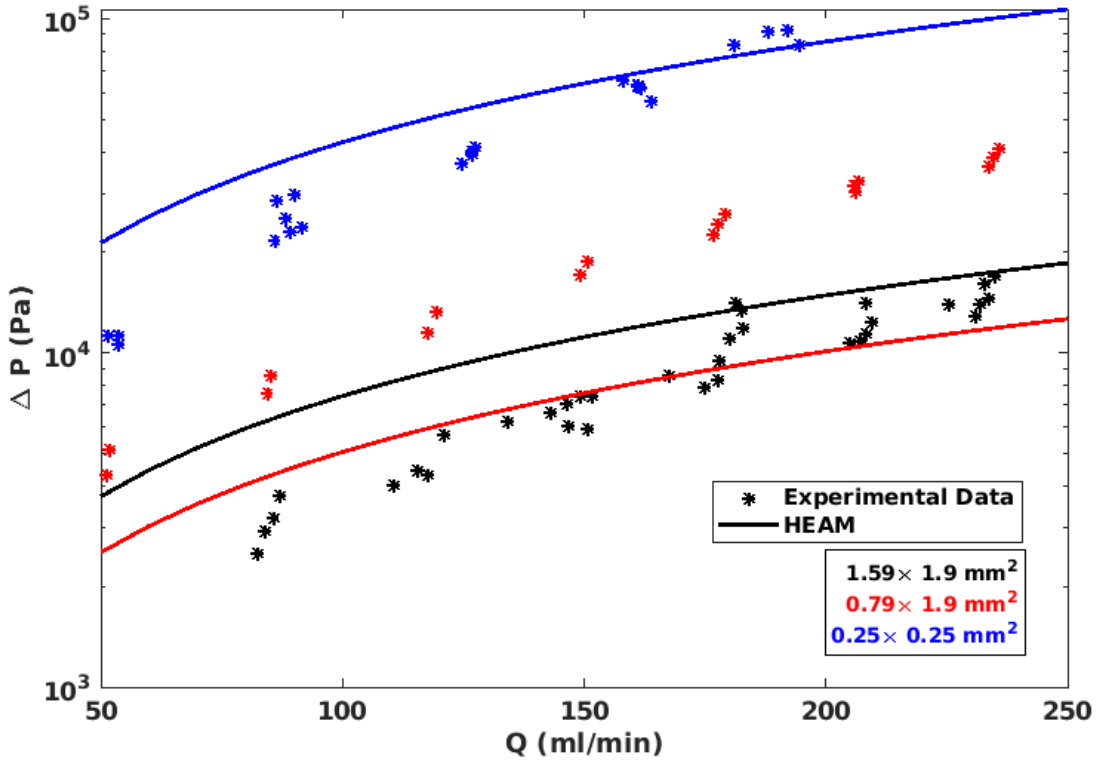


Figure 3. 16. Experimental and predicted pressure drop for IFFs with different channel dimensions by HEAM. (Blue: 0.25 mm× 0.25 mm- 10 parallel channels, Red: 0.79 mm× 1.9 mm- 6 parallel channels, Black: 1.59 mm× 1.9 mm- 4 parallel channels). It predicts correct trends for the change in pressure drop with different channel area for blue and black, and blue and red cases; however, it cannot predict the same relationship for black and red case correctly.

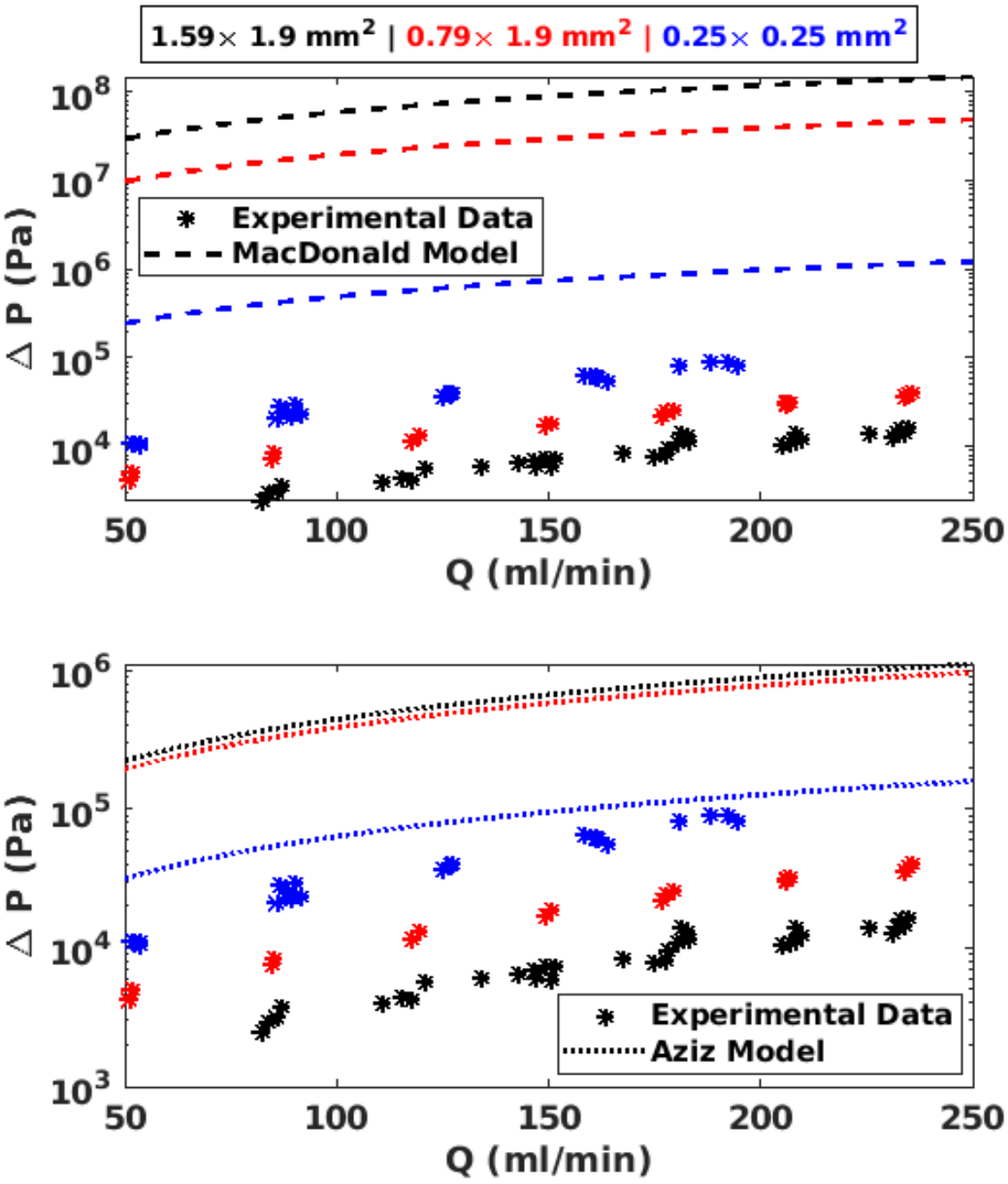


Figure 3. 17. Experimental and predicted pressure drop for IFFs with different channel dimensions by Messaggi and Aziz models. (Blue: 0.25 mm× 0.25 mm- 10 parallel channels, Red: 0.79 mm× 1.9 mm- 6 parallel channels, Black: 1.59 mm× 1.9 mm- 4 parallel channels) Both models predict a false trend for the change in pressure drop with different channel area.

### 3.8.2- Improving flow distribution in IFFs

Figure 3. 18 illustrates the flow share of each channel in an RFB with 10-channels IFF, described in [38] with 0.25 mm wide channels. This figure acknowledges the non-uniformity in the flow distribution between channels. It encompasses multiple suggestions to improve the flow distribution in RFBs with IFF design, as designing wider manifold, shorter channels, more compressed electrodes, and wider ribs. All the suggestions show more uniform flow distributions than the original flow field design, promising better cell performances.

In general, the HEAM recommends that any modification, leading to increase in the difference between the manifold viscous resistance and channels resistance, helps the flow distribution. Therefore, modifications to improve the flow distribution in IFF designs are designing wider manifold, wider ribs, shorter channels, and further compressing electrodes. However, these modifications, excluding utilizing wider manifolds, increase the viscous resistance, hence, the overall pressure drop. This increase in the pressure drop is not desired, therefore, the best option to improve the flow distribution in IFF designs is to use wider flow distribution manifolds.

These results are consistent with the literature. Maurya et. al discovered that using carbon paper instead of carbon felts improves the flow distribution in VRFBs with IFF, which resulted in higher power density for VRFBs using carbon papers than the ones utilizing carbon felts. [49] The afore-mentioned article does not mention the reasoning behind the phenomena, but the HEAM predicts that higher electrode compressibility and lower electrode permeability are the cause of it, aligned with the results of the article. Skyllas-Kazacos group discovered that the flow distribution between VRFB cells, while stacked, is more uniform where the pressure drop in each cell is higher. Additionally, the flow is distributed more evenly when wider flow distribution manifold is utilized.

[85] These results are consistent with the approach of the HEAM towards the flow distribution in RFBs with IFF designs . Through these analyses, Objective 3 is accomplished.

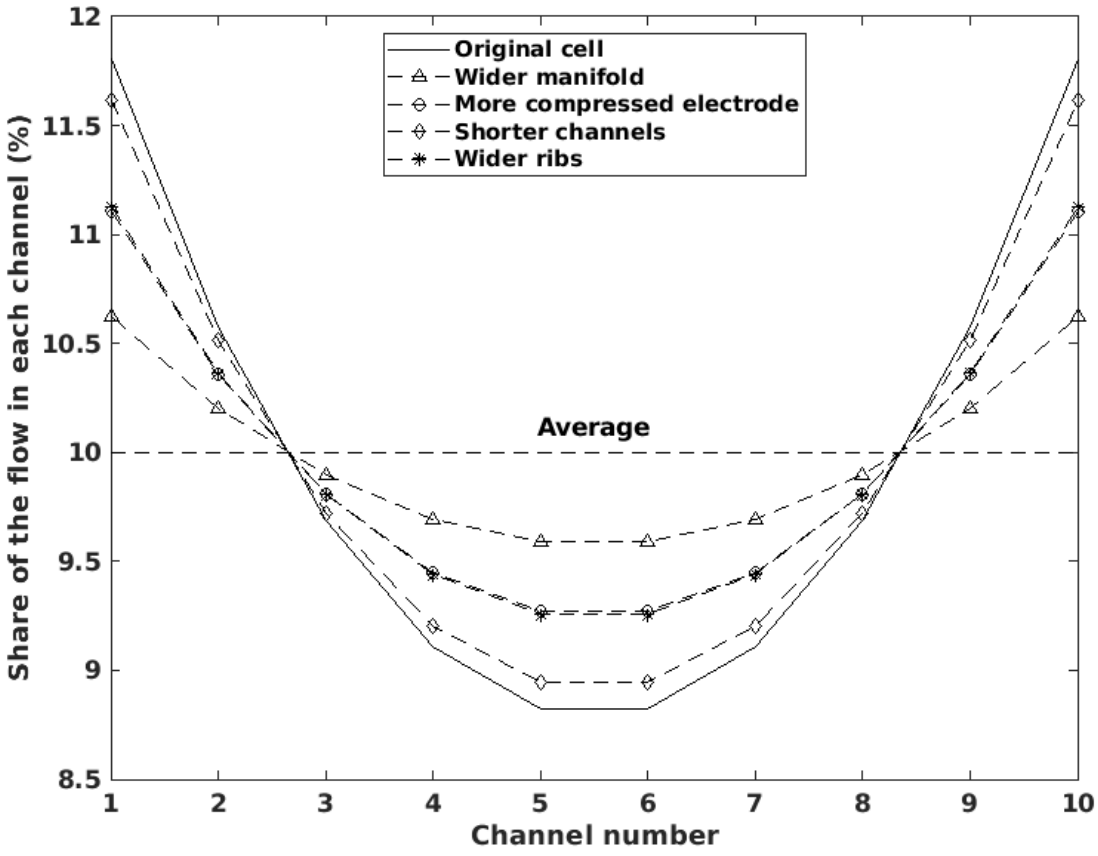


Figure 3. 18. Normalized flow distribution for the 0.25 mm wide channels IFF in Aziz article [38]. The improvements for each case are a. Changing the manifold width from 0.25 mm to 0.5 mm. b. Compression of the electrode where its permeability and thickness decreases to $1\times10^{-11}$ $m^2$ and 0.143 mm, respectively. c. 15 cm long channels instead of 19 cm long channels. d. the width of the ribs and channels change from 0.79 mm and 0.25 mm to 0.85 mm and 0.19 mm, respectively. In all cases, the projected flow distribution is improved.

3.8.3- The overall pressure drop for RFBs with different FF designs

Figure 3. 19-19 illustrate the overall pressure drop prediction of HEAM for the designed experiments, and the data for the pressure drop of RFBs in Messaggi's article. [43] All the compared FFs have the same active area and channel size. These figures demonstrate that RFBs with IFF designs cause the least pressure drop among the three studied designs. This result is consistent with different flow rates. Therefore, it is concluded that RFBs with IFF designs require lower pump work, hence, have an advantage over RFBs with SFF designs. Objective 4 is accomplished through these analyses.

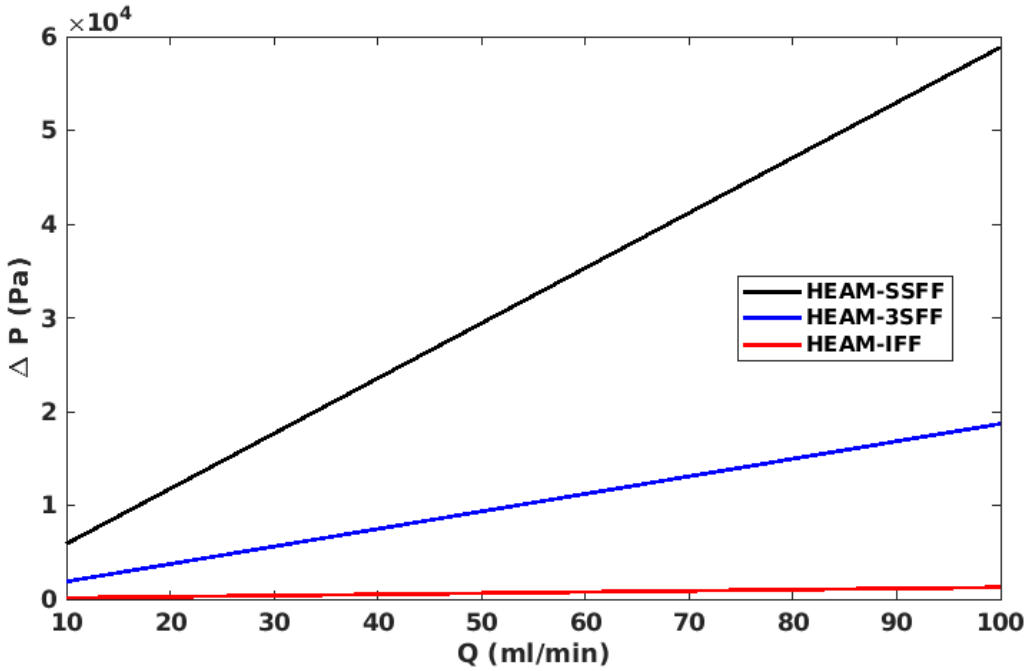


Figure 3. 19. Comparison of the pressure drop for different flow field designs with the same active and channel cross-sectional area. The HEAM predicts that the pressure drop of RFBs with IFF design is lower than the similar with SSFF and MSFF designs.

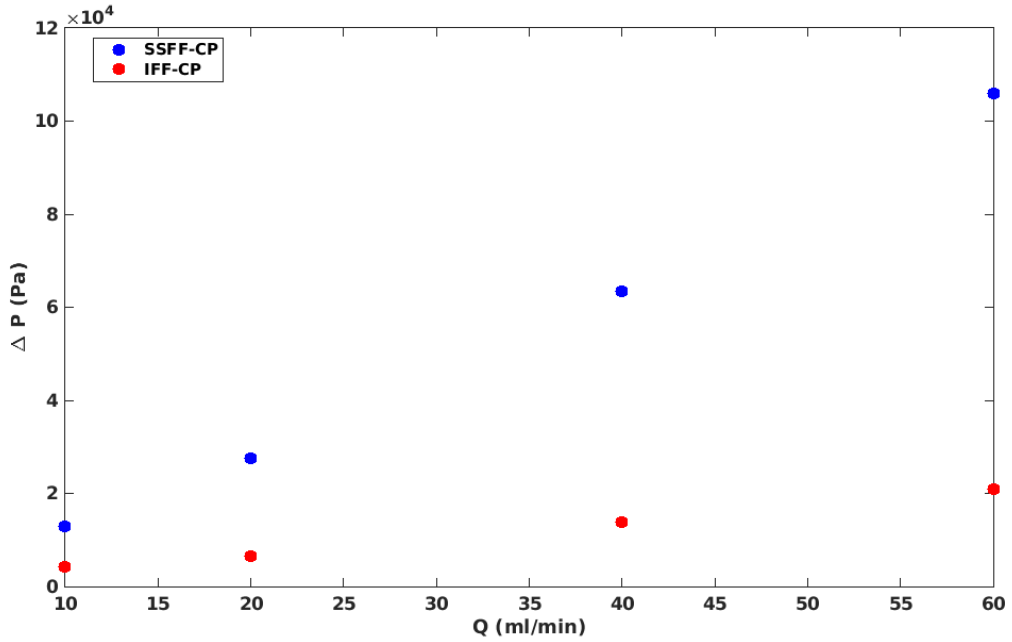


Figure 3. 20. Comparison of the pressure drop for different flow field designs with the same active and channel cross-sectional area for the data from Messaggi's article. [43] This plot suggests pressure drop along RFBs with IFF is lower than the similar with SSFF.

3.8.4- Analysis of the effect of different DNs on the overall pressure drop

Identifying the dimensionless parameters and the dependence of pressure drop on them is important for RFB cell design while stacking and scaling up. The HEAM is a tool to understand these dependences, therefore, it is utilized to demonstrate the relationship between the pressure drop and effective dimensionless numbers. The main assumption for the cases that are not fitted to experimental data is that the C-values remain the same for different scenarios using the same electrode or the same FF design. This assumption is a weak one, which can be strengthened by implementing more experimental data and extracting C-values for each case. Nevertheless, the results presented from implementing the HEAM gives useful insights on the impact of each dimensionless number on the pressure drop.

Euler number is the dimensionless number representing the pressure drop. However, plotting it does not give valuable visual information due to the presence of velocity components in its denominator. Therefore, the pressure drop is presented as the dependent variable in the upcoming figures.

3.8.4.1- The Reynolds number

As Figure 3. 21 demonstrates, RFB cells utilizing carbon paper cause more pressure drop than RFB cells using carbon felts. This result is consistent with different Reynolds numbers and FFs. It is justified as the permeability and porosity of the carbon paper is less than the carbon felt, therefore, diffusing in the carbon paper requires more hydraulic pressure than the carbon felts. Additionally, the maximum Reynolds number in the channels for all the FFs is 700, far from the transition region, which starts at Reynolds number of 2100. It is another evidence for the strength of assuming laminar flow in the channels of the cells.

Figure 3. 22 illustrates the pressure drop for different flow fields utilizing the same electrode. RFB cells with carbon felts seems to have the same trendline, as different FFs have comparable pressure drop values at the same Reynolds number. However, RFB cells with SSFF are predicted to have different trendline than the ones with IFFs or 3SFFs utilizing carbon paper. This plot implies that in case of having a threshold for the Reynolds number while designing an RFB system, IFFs and MSFFs require lower pump workload than SSFFs to operate.

3.8.4.2- The electrode permeability

Figure 3. 23 demonstrates the predicted pressure drop for different FFs and electrodes with various electrode compression ratios (CRs- from 10% to 50%). All the setups, except for IFF-CP case, do not expect notable changes in their pressure drop while compressed. It shows that the CR effects

thinner electrodes more than the thicker ones for RFB cells with IFF due to the higher mean velocity above the ribs, hence, significantly increasing the pressure drop with more electrode compression. Additionally, this result illustrates the dominancy of the pressure drop above the ribs while utilizing carbon papers.

However, it cannot be concluded that the compression ratio does not affect the pressure drop for all the cases due to the absence of C-value tuning of the channels pressure modeling for different setups. The C-value is subject to change when the electrode compression ratio varies. Therefore, experimental data is required to modify the C-values and assure the validity of this result. However, it is expected to observe increase in C-value in case of higher compression ratio due to the difficulty of diffusing in more compressed electrodes.

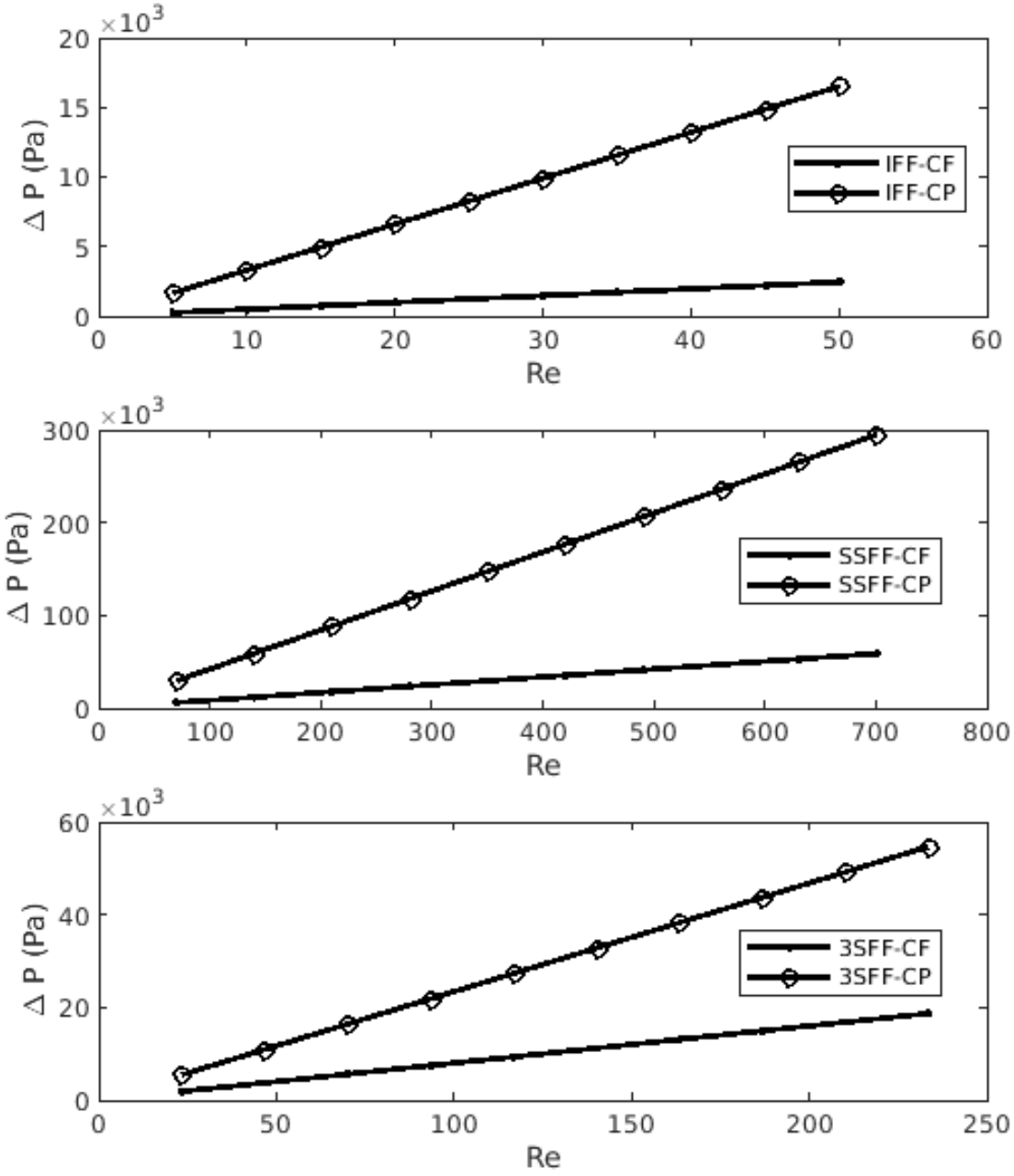


Figure 3. 21. The pressure drop for different electrodes utilized at the same flow fields in their corresponding Reynolds number range. It is evident that in all cases, cells utilizing carbon paper require more pressure drop for the cell to operate.

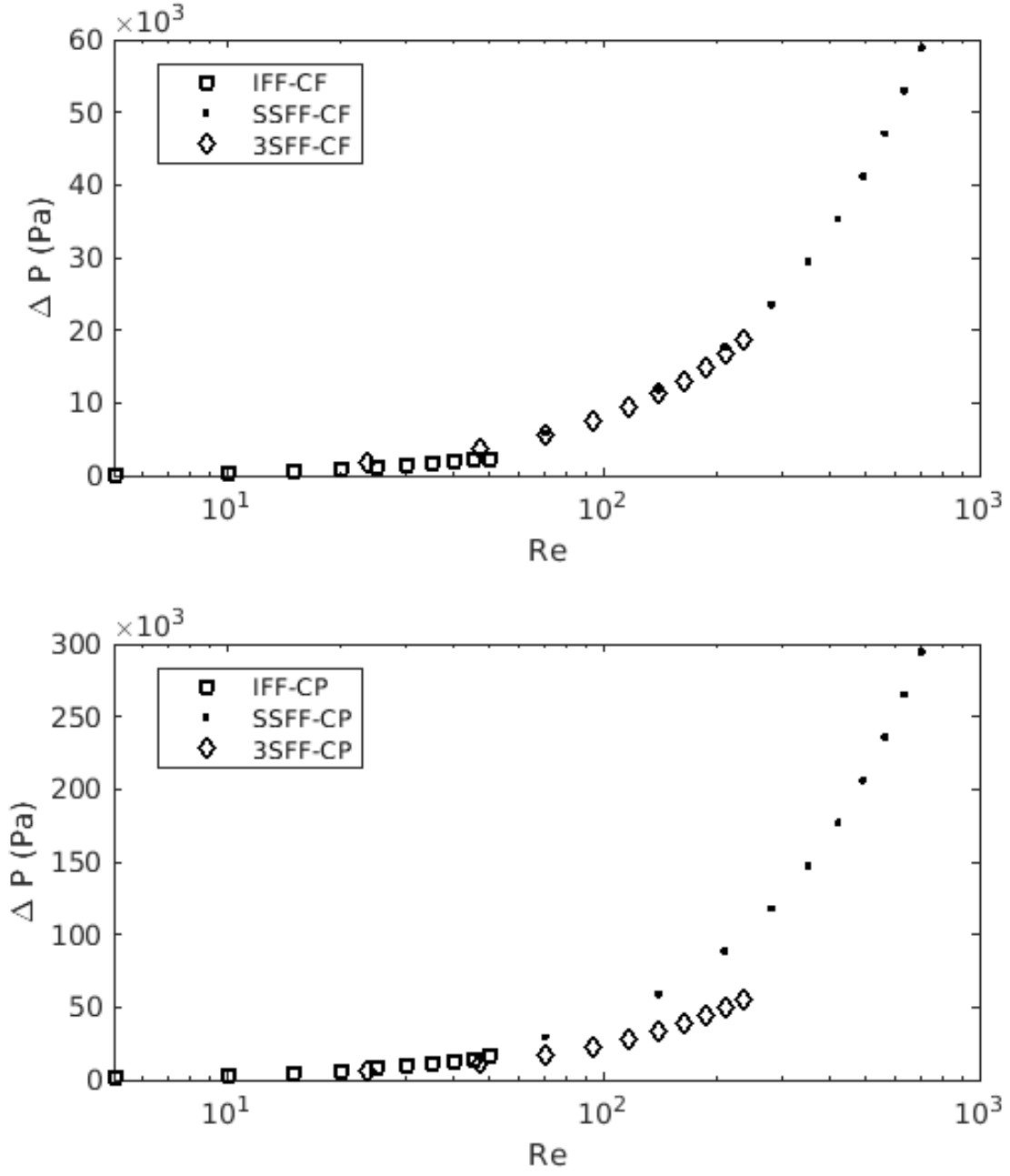


Figure 3. 22. The pressure drop for different flow fields utilizing the same electrode in their corresponding Reynolds number range. The pressure drop at all the flow fields utilizing carbon felts are comparable to each other at the same Reynolds number, however, it seems IFFs and 3SFFs cause less pressure drop at the same Reynolds number compared to SSFF.

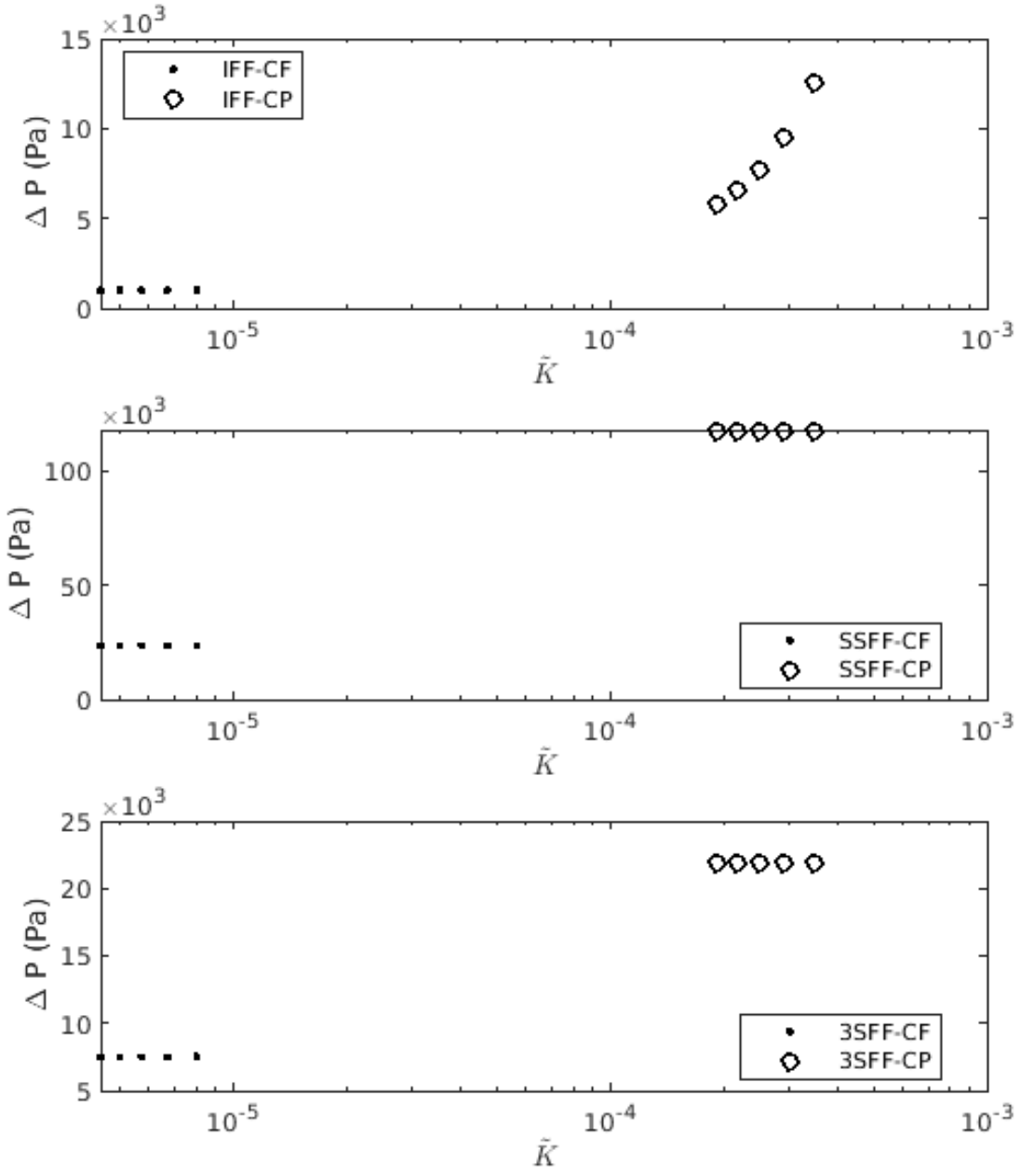


Figure 3. 23. The pressure drop for different flow fields and electrodes with compression ratio of 10%, 20%, 30%, 40% and 50%. Except for the IFF-CP case, all cases are indifferent to the compression ratio. Increase in the pressure drop with the increase in CR is demonstrated for the IFF-CP case.

3.8.4.3- The height of the channels

As Figure 3. 24 demonstrates, the predicted pressure drop decreases with the increase in the height of the channels for every FF and electrode design. It is due to the increase in the hydraulic diameter of the channels; hence, the fluid has more space to flow through. Additionally, as Equation 3.30 suggests, higher ratio of channel height and width leads to lower C-values. Therefore, it is expected for the C-value to intensify the observed trend between the height of the channels and the pressure drop.

3.8.4.4- The width of the ribs

Figure 3. 25 demonstrates the pressure drop for different FFs and electrodes with various ribs width. It is assumed that the active area of the RFB cells is the same in each case, therefore, the summation of channels and ribs width remains the same (2 mm). As Figure 3. 25 suggests, the predicted pressure drop increases with the increase in the width of the ribs for every FF and electrode design. This result is justified by the decrease in the hydraulic diameter of the channels and the increase in the length that the flow is required to jump over the ribs. Additionally, as Equation 3.30 suggests, higher ratio of channel width and height leads to higher C-values. Therefore, it is expected for the C-value to intensify the observed trend between the width of the ribs and the pressure drop. Through these analyses, Objective 1 is obtained.

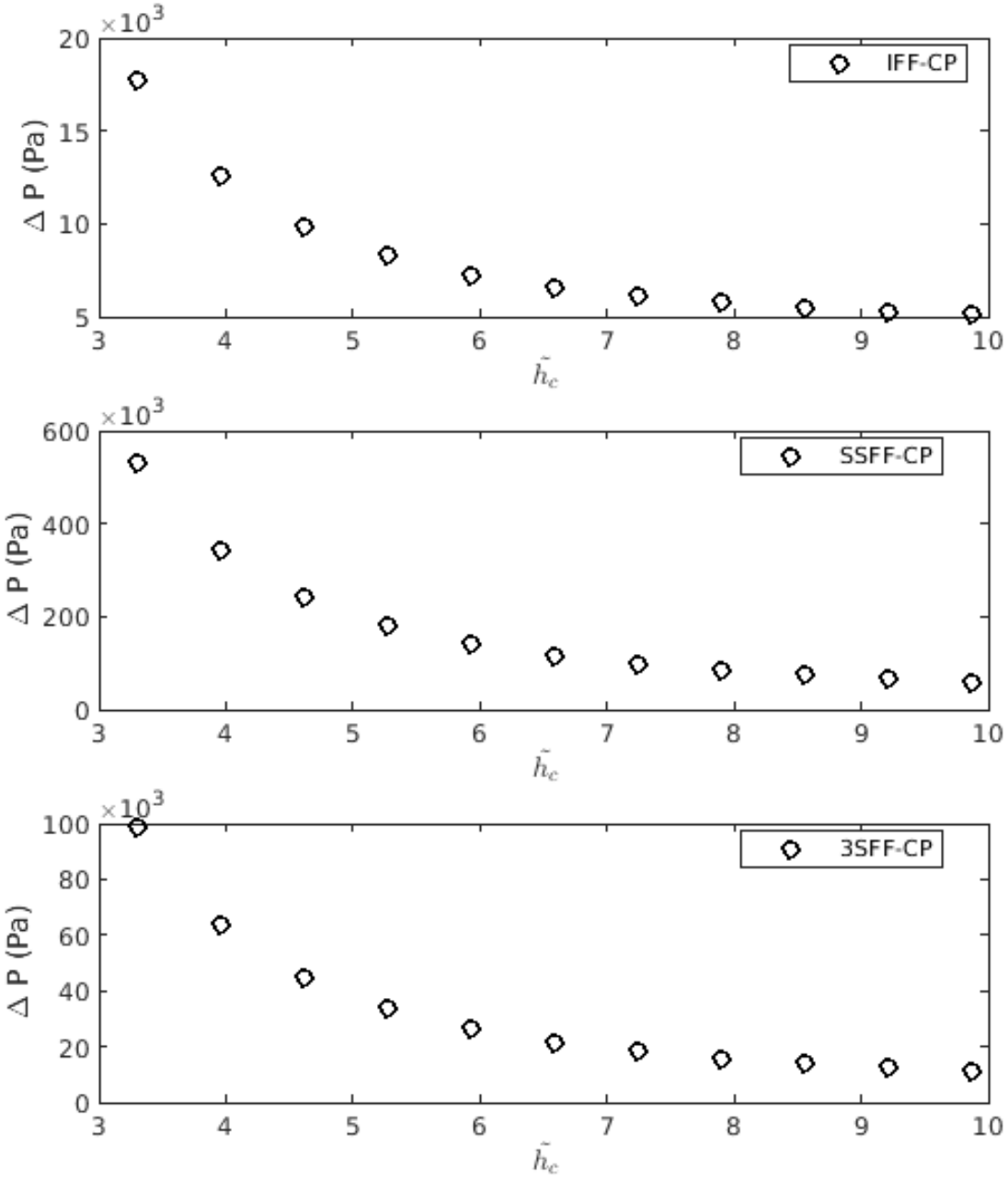


Figure 3. 24. The pressure drop for different flow fields and electrodes with different channel heights. As the channel height increases, the pressure drop decreases.

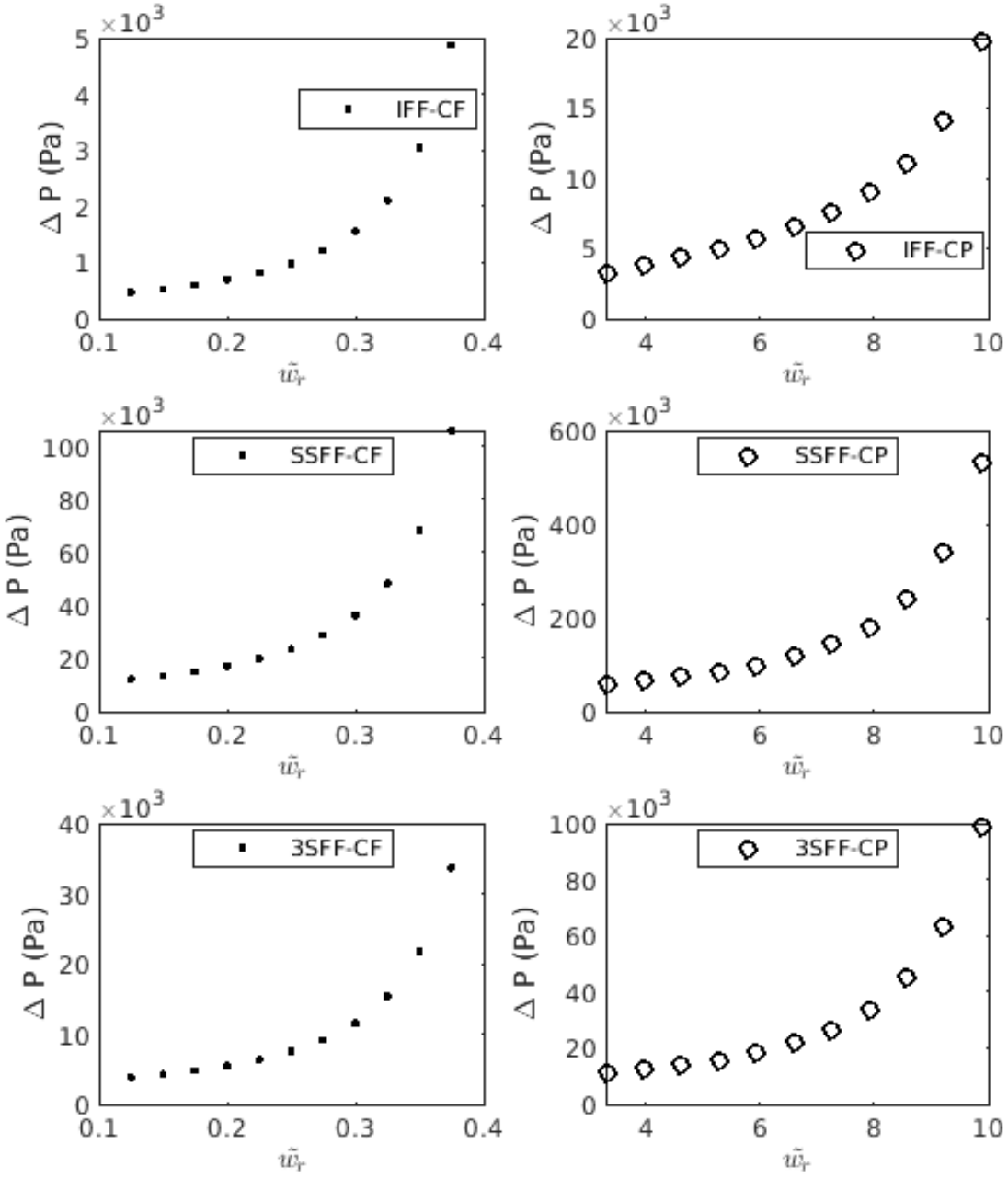


Figure 3. 25. The pressure drop for different flow fields and electrodes with different channels and ribs width. As the ribs width increases, the pressure drop increases.

# Chapter 4- Conclusions and future directions

## 4.1- Conclusions

A main inefficiency of RFBs with IFF design is their non-uniform flow distribution. Moreover, a major inquiry while scaling up RFBs is electrolytes pump capacity, an energy sink for the system. Flow field designs influence both flow distribution and pump power consumption rate. Investigating their effect on the afore-mentioned issues is the first step to improve their design. The present study focuses on the hydrodynamic aspects of flow fields and provides a model to examine the pressure distribution in RFBs.

The important parameters effective on the pressure drop in RFB systems is identified, and six corresponding dimensionless numbers are extracted. These dimensionless numbers are integral to designing, controlling, and comparing RFB systems.

A model, abbreviated as HEAM, is developed by implementing scaling analysis to predict the pressure drop and pressure distribution for any flow field design. The accuracy of HEAM is compared to other analytical and CFD models available in the literature. HEAM has proven to be accurate in predicting pressure drop for RFBs with SFF design and inconsistent in doing the same for RFBs with IFF design. However, it is more accurate than other analytical models, and its accuracy is comparable to computationally-costly CFD models. Therefore, it is more reliable than its competitive models for further analysis.

HEAM predicts the non-uniformity of the flow distribution in channels of IFF design. Moreover, it suggests multiple solutions to relax the non-uniformity. These modifications were supported by the literature. The best suggestion is to design wider manifolds, which improves flow distribution and reduces overall pressure drop. Additionally, it predicts that RFBs with IFF cause lower pressure drop than the ones with SFF design. This result is in favor of IFFs, giving them an

advantage over SFFs. However, this hydrodynamic analysis needs to be coupled with electrochemical performance of each flow field to obtain the most efficient flow field for each application.

## 4.2- Future directions

The HEAM is developed by using a linear relationship between the pressure drop and the flow rate. Several publications suggest a parabolic equation using friction factor and dimensionless numbers to predict pressure drop. [55,76,85] The friction factor is defined to be inversely proportional to the flow rate in laminar flow regime to preserve the linear relationship between the pressure drop and the flow rate. However, this approach has the benefit to be more flexible when there are non-linearity in the data due to turbulence. [87] Integrating this approach to the HEAM enhances its accuracy. However, non-linearities between the pressure drop and the flow rate complicates the HEAM linear approach to this relationship. It needs to be overcome by changing the approach of the model.

The modeling in porous media deviates from experimental data and is a cause for inaccuracy in predicting IFF pressure drop. Finding more sophisticated models for porous media is a goal that requires intense literature review and testing different models with experimental data that can be performed in the future.

In this study, six dimensionless numbers to describe the hydrodynamic of RFB cells are identified and their effect on the pressure drop is investigated. However, the C-value for each case is not tuned due to the absence of data. The next step will be to carefully design experiments to find the change in C-value and implement it in the model for different scenarios. Behavior of dimensionless numbers gives insights into behavior of electrolyte flow inside RFB cells. Additionally, the results from experimental studies can be utilized in large-scale applications of RFB systems.

The HEAM predicts the behavior of electrolyte flow in RFBs. This model can be integrated with analytical kinetics model to predict the electrochemical performance of RFB systems. The integrated model can quantify pump power consumption rate and RFB power generation rate and provide an optimized flow field design for every application.

## References


[1] L.L.N. Laboratory, Energy Flow Charts, (n.d.). https://flowcharts.llnl.gov/commodities/energy (accessed June 30, 2020).

[2] G.L. Soloveichik, Flow Batteries: Current Status and Trends, Chem. Rev. 115 (2015) 11533–11558. https://doi.org/10.1021/cr500720t.

[3] L. Li, S. Kim, W. Wang, M. Vijayakumar, Z. Nie, B. Chen, J. Zhang, G. Xia, J. Hu, G. Graff, J. Liu, Z. Yang, A stable vanadium redox-flow battery with high energy density for large-scale energy storage, Adv. Energy Mater. 1 (2011) 394–400. https://doi.org/10.1002/aenm.201100008.

[4] K. Mongird, V. Fotedar, V. Viswanathan, V. Koritarov, P. Balducci, B. Hadjerioua, J. Alam, Energy Storage Technology and Cost Characterization Report, 2019. https://www.energy.gov/sites/prod/files/2019/07/f65/Storage Cost and Performance Characterization Report_Final.pdf (accessed November 30, 2020).

[5] P. Alotto, M. Guarnieri, F. Moro, Redox flow batteries for the storage of renewable energy: A review, Renew. Sustain. Energy Rev. 29 (2014) 325–335. https://doi.org/10.1016/j.rser.2013.08.001.

[6] S. Selverston, E. Nagelli, J.S. Wainright, R.F. Savinell, All-Iron Hybrid Flow Batteries with In-Tank Rebalancing, J. Electrochem. Soc. 166 (2019) A1725–A1731. https://doi.org/10.1149/2.0281910jes.

[7] Y. Yang, G. Zheng, Y. Cui, A membrane-free lithium/polysulfide semi-liquid battery for large-scale energy storage, Energy Environ. Sci. 6 (2013) 1552–1558. https://doi.org/10.1039/c3ee00072a.

[8] R.M. Darling, K.G. Gallagher, J.A. Kowalski, S. Ha, F.R. Brushett, Pathways to low-cost electrochemical energy storage: A comparison of aqueous and nonaqueous flow batteries, Energy Environ. Sci. 7 (2014) 3459–3477. https://doi.org/10.1039/c4ee02158d.

[9] M.L. Perry, J.D. Saraidaridis, R.M. Darling, Crossover mitigation strategies for redox-flow batteries, Curr. Opin. Electrochem. 21 (2020) 311–318. https://doi.org/10.1016/j.coelec.2020.03.024.

[10] S. Roe, C. Menictas, M. Skyllas-Kazacos, A High Energy Density Vanadium Redox Flow Battery with 3 M Vanadium Electrolyte, J. Electrochem. Soc. 163 (2016) A5023–A5028. https://doi.org/10.1149/2.0041601jes.

[11] T.F. Fuller, J.N. Harb, Electrochemical Engineering, 1st ed., John Wiley & Sons, Inc., 2018.

[12] N. Yun, J.J. Park, O.O. Park, K.B. Lee, J.H. Yang, Electrocatalytic effect of NiO nanoparticles evenly distributed on a graphite felt electrode for vanadium redox flow batteries, Electrochim. Acta. 278 (2018) 226–235. https://doi.org/10.1016/j.electacta.2018.05.039.

[13] M.H. Chakrabarti, N.P. Brandon, S.A. Hajimolana, F. Tariq, V. Yufit, M.A. Hashim, M.A. Hussain, C.T.J. Low, P. V. Aravind, Application of carbon materials in redox flow batteries, J. Power Sources. 253 (2014) 150–166. https://doi.org/10.1016/j.jpowsour.2013.12.038.

[14] K.J. Kim, Y.J. Kim, J.H. Kim, M.S. Park, The effects of surface modification on carbon felt electrodes for use in vanadium redox flow batteries, Mater. Chem. Phys. 131 (2011) 547–553. https://doi.org/10.1016/j.matchemphys.2011.10.022.

[15] S. Wang, X. Zhao, T. Cochell, A. Manthiram, Nitrogen-doped carbon nanotube/graphite felts as advanced electrode materials for vanadium redox flow batteries, J. Phys. Chem. Lett. 3 (2012) 2164–2167. https://doi.org/10.1021/jz3008744.

[16] V. Pasala, J.N. Ramavath, C. He, V.K. Ramani, K. Ramanujam, N- and P-co-doped Graphite Felt Electrode for Improving Positive Electrode Chemistry of the Vanadium Redox Flow Battery, ChemistrySelect. 3 (2018) 8678–8687. https://doi.org/10.1002/slct.201801446.

[17] C. Gao, N. Wang, S. Peng, S. Liu, Y. Lei, X. Liang, S. Zeng, H. Zi, Influence of Fenton's reagent treatment on electrochemical properties of graphite felt for all vanadium redox flow battery, Electrochim. Acta. 88 (2013) 193–202. https://doi.org/10.1016/j.electacta.2012.10.021.

[18] B. Sun, M. Skyllas-Kazacos, Chemical modification of graphite electrode materials for vanadium redox flow battery application-part II. Acid treatments, Electrochim. Acta. 37 (1992) 2459–2465. https://doi.org/10.1016/0013-4686(92)87084-D.

[19] M. Etienne, J.F. Vivo-Vilches, I. Vakulko, C. Genois, L. Liu, M. Perdicakis, R. Hempelmann, A. Walcarius, Layer-by-Layer modification of graphite felt with MWCNT for vanadium redox flow battery, Electrochim. Acta. 313 (2019) 131–140. https://doi.org/10.1016/j.electacta.2019.04.022.

[20] Y.S. Chou, K.T. Jeng, S.C. Yen, Characterization and electrochemical properties of graphite felt-based electrode modified using an ionomer impregnation approach for vanadium redox flow battery, Electrochim. Acta. 251 (2017) 109–118. https://doi.org/10.1016/j.electacta.2017.08.064.

[21] A. Xu, L. Shi, L. Zeng, T.S. Zhao, First-principle investigations of nitrogen-, boron-, phosphorus-doped graphite electrodes for vanadium redox flow batteries, Electrochim. Acta. 300 (2019) 389–395. https://doi.org/10.1016/j.electacta.2019.01.109.

[22] A.B. Shah, Y. Wu, Y.L. Joo, Direct addition of sulfur and nitrogen functional groups to graphite felt electrodes for improving all-vanadium redox flow battery performance, Electrochim. Acta. 297 (2019) 905–915. https://doi.org/10.1016/j.electacta.2018.12.052.

[23] B. Sun, M. Skyllas-Kazacos, Modification of graphite electrode materials for vanadium redox flow battery application-I. Thermal treatment, Electrochim. Acta. 37 (1992) 1253–1260. https://doi.org/10.1016/0013-4686(92)85064-R.

[24] W. Zhang, J. Xi, Z. Li, H. Zhou, L. Liu, Z. Wu, X. Qiu, Electrochemical activation of graphite felt electrode for VO 2+/VO2+ redox couple application, Electrochim. Acta. 89 (2013) 429–435. https://doi.org/10.1016/j.electacta.2012.11.072.

[25] Y. Shen, H. Xu, P. Xu, X. Wu, Y. Dong, L. Lu, Electrochemical catalytic activity of tungsten trioxide- Modified graphite felt toward VO2+/VO2+ redox reaction, Electrochim. Acta. 132 (2014) 37–41. https://doi.org/10.1016/j.electacta.2014.03.107.

[26] H.T. Thu Pham, C. Jo, J. Lee, Y. Kwon, MoO2 nanocrystals interconnected on mesocellular carbon foam as a powerful catalyst for vanadium redox flow battery, RSC Adv. 6 (2016) 17574–17582. https://doi.org/10.1039/c5ra24626a.

[27] H. Zhou, J. Xi, Z. Li, Z. Zhang, L. Yu, L. Liu, X. Qiu, L. Chen, CeO2 decorated graphite felt as a high-performance electrode for vanadium redox flow batteries, RSC Adv. 4 (2014) 61912–61918. https://doi.org/10.1039/c4ra12339e.

[28] H. Zhou, Y. Shen, J. Xi, X. Qiu, L. Chen, ZrO2-Nanoparticle-Modified Graphite Felt: Bifunctional Effects on Vanadium Flow Batteries, ACS Appl. Mater. Interfaces. 8 (2016) 15369–15378. https://doi.org/10.1021/acsami.6b03761.

[29] D.M. Kabtamu, J.Y. Chen, Y.C. Chang, C.H. Wang, Electrocatalytic activity of Nb-doped hexagonal WO3 nanowire-modified graphite felt as a positive electrode for vanadium redox flow batteries, J. Mater. Chem. A. 4 (2016) 11472–11480. https://doi.org/10.1039/c6ta03936g.

[30] L. Gubler, Membranes and separators for redox flow batteries, Curr. Opin. Electrochem. 18 (2019) 31–36. https://doi.org/10.1016/j.coelec.2019.08.007.

[31] L. Zeng, T.S. Zhao, L. Wei, H.R. Jiang, M.C. Wu, Anion exchange membranes for aqueous acid-based redox flow batteries: Current status and challenges, Appl. Energy. 233–234 (2019) 622–643. https://doi.org/10.1016/j.apenergy.2018.10.063.

[32] A.M. Pezeshki, Z.J. Tang, C. Fujimoto, C.-N. Sun, M.M. Mench, T.A. Zawodzinski, Full Cell Study of Diels Alder Poly(phenylene) Anion and Cation Exchange Membranes in Vanadium Redox Flow Batteries, J. Electrochem. Soc. 163 (2016) A5154–A5162. https://doi.org/10.1149/2.0201601jes.

[33] Z. Tang, J.S. Lawton, C.-N. Sun, J. Chen, M.I. Bright, A.M. Jones, A.B. Papandrew, C.H. Fujimoto, T.A. Zawodzinski, Characterization of Sulfonated Diels-Alder Poly(phenylene) Membranes for Electrolyte Separators in Vanadium Redox Flow Batteries, J. Electrochem. Soc. 161 (2014) A1860–A1868. https://doi.org/10.1149/2.0631412jes.

[34] G. Hu, Y. Wang, J. Ma, J. Qiu, J. Peng, J. Li, M. Zhai, A novel amphoteric ion exchange membrane synthesized by radiation-induced grafting α-methylstyrene and N,N-

dimethylaminoethyl methacrylate for vanadium redox flow battery application, J. Memb. Sci. 407–408 (2012) 184–192. https://doi.org/10.1016/j.memsci.2012.03.042.

[35] M. Jung, W. Lee, N. Nambi Krishnan, S. Kim, G. Gupta, L. Komsiyska, C. Harms, Y. Kwon, D. Henkensmeier, Porous-Nafion/PBI composite membranes and Nafion/PBI blend membranes for vanadium redox flow batteries, Appl. Surf. Sci. 450 (2018) 301–311. https://doi.org/10.1016/j.apsusc.2018.04.198.

[36] J. Dai, Y. Dong, P. Gao, J. Ren, C. Yu, H. Hu, Y. Zhu, X. Teng, A sandwiched bipolar membrane for all vanadium redox flow battery with high coulombic efficiency, Polymer (Guildf). 140 (2018) 233–239. https://doi.org/10.1016/j.polymer.2018.02.051.

[37] S. Kim, S. Yuk, H.G. Kim, C. Choi, R. Kim, J.Y. Lee, Y.T. Hong, H.T. Kim, A hydrocarbon/Nafion bilayer membrane with a mechanical nano-fastener for vanadium redox flow batteries, J. Mater. Chem. A. 5 (2017) 17279–17286. https://doi.org/10.1039/c7ta02921g.

[38] M.R. Gerhardt, A.A. Wong, M.J. Aziz, The Effect of Interdigitated Channel and Land Dimensions on Flow Cell Performance, J. Electrochem. Soc. 165 (2018) A2625–A2643. https://doi.org/10.1149/2.0471811jes.

[39] X. Ke, J.M. Prahl, I.J.D. Alexander, J.S. Wainright, T.A. Zawodzinski, R.F. Savinell, Rechargeable redox flow batteries: Flow fields, stacks and design considerations, Chem. Soc. Rev. 47 (2018) 8721–8743. https://doi.org/10.1039/c8cs00072g.

[40] Q. Xu, T.S. Zhao, C. Zhang, Performance of a vanadium redox flow battery with and without flow fields, Electrochim. Acta. 142 (2014) 61–67. https://doi.org/10.1016/j.electacta.2014.07.059.

[41] S. Maurya, P.T. Nguyen, Y.S. Kim, Q. Kang, R. Mukundan, Effect of flow field geometry on operating current density, capacity and performance of vanadium redox flow battery, J. Power Sources. 404 (2018) 20–27. https://doi.org/10.1016/j.jpowsour.2018.09.093.

[42] E. Knudsen, P. Albertus, K.T. Cho, A.Z. Weber, A. Kojic, Flow simulation and analysis of high-power flow batteries, J. Power Sources. 299 (2015) 617–628. https://doi.org/10.1016/j.jpowsour.2015.08.041.

[43] M. Messaggi, P. Canzi, R. Mereu, A. Baricci, F. Inzoli, A. Casalegno, M. Zago, Analysis of flow field design on vanadium redox flow battery performance: Development of 3D computational fluid dynamic model and experimental validation, Appl. Energy. 228 (2018) 1057–1070. https://doi.org/10.1016/j.apenergy.2018.06.148.

[44] S. Kumar, S. Jayanti, Effect of electrode intrusion on pressure drop and electrochemical performance of an all-vanadium redox flow battery, J. Power Sources. 360 (2017) 548–558. https://doi.org/10.1016/j.jpowsour.2017.06.045.

[45] C.R. Dennison, E. Agar, B. Akuzum, E.C. Kumbur, Enhancing Mass Transport in Redox Flow Batteries by Tailoring Flow Field and Electrode Design, J. Electrochem. Soc. 163 (2016) A5163–A5169. https://doi.org/10.1149/2.0231601jes.

[46] J. Houser, J. Clement, A. Pezeshki, M.M. Mench, Influence of architecture and material properties on vanadium redox flow battery performance, J. Power Sources. 302 (2016) 369–377. https://doi.org/10.1016/j.jpowsour.2015.09.095.

[47] M. Messaggi, C. Rabissi, C. Gambaro, L. Meda, A. Casalegno, M. Zago, Investigation of vanadium redox flow batteries performance through locally-resolved polarisation curves and impedance spectroscopy: Insight into the effects of electrolyte, flow field geometry

and electrode thickness, J. Power Sources. 449 (2020) 227588. https://doi.org/10.1016/j.jpowsour.2019.227588.

[48] Y.K. Zeng, X.L. Zhou, L. Zeng, X.H. Yan, T.S. Zhao, Performance enhancement of iron-chromium redox flow batteries by employing interdigitated flow fields, J. Power Sources. 327 (2016) 258–264. https://doi.org/10.1016/j.jpowsour.2016.07.066.

[49] S. Maurya, P.T. Nguyen, Y.S. Kim, Q. Kang, R. Mukundan, Effect of flow field geometry on operating current density, capacity and performance of vanadium redox flow battery, J. Power Sources. 404 (2018) 20–27. https://doi.org/10.1016/j.jpowsour.2018.09.093.

[50] J.T. Clement, D.S. Aaron, M.M. Mench, In Situ Localized Current Distribution Measurements in All-Vanadium Redox Flow Batteries, J. Electrochem. Soc. 163 (2016) A5220–A5228. https://doi.org/10.1149/2.0241601jes.

[51] T.Y. Ertugrul, J.T. Clement, Y.A. Gandomi, D.S. Aaron, M.M. Mench, In-situ current distribution and mass transport analysis via strip cell architecture for a vanadium redox flow battery, J. Power Sources. 437 (2019) 226920. https://doi.org/10.1016/j.jpowsour.2019.226920.

[52] W.Y. Hsieh, C.H. Leu, C.H. Wu, Y.S. Chen, Measurement of local current density of all-vanadium redox flow batteries, J. Power Sources. 271 (2014) 245–251. https://doi.org/10.1016/j.jpowsour.2014.06.081.

[53] E. García-Quismondo, I. Almonacid, M.Á.C. Martínez, V. Miroslavov, E. Serrano, J. Palma, J.P.A. Salmerón, Operational experience of 5 kW/5 kWh all-vanadium flow batteries in photovoltaic grid applications, Batteries. 5 (2019) 52. https://doi.org/10.3390/batteries5030052.

[54] M. Schreiber, M. Harrer, A. Whitehead, H. Bucsich, M. Dragschitz, E. Seifert, P. Tymciw, Practical and commercial issues in the design and manufacture of vanadium flow batteries, J. Power Sources. 206 (2012) 483–489. https://doi.org/10.1016/j.jpowsour.2010.12.032.

[55] A. Tang, J. Bao, M. Skyllas-Kazacos, Studies on pressure losses and flow rate optimization in vanadium redox flow battery, J. Power Sources. 248 (2014) 154–162. https://doi.org/10.1016/j.jpowsour.2013.09.071.

[56] G. Merei, S. Adler, D. Magnor, M. Leuthold, D.U. Sauer, Multi-physics model for a vanadium redox flow battery, Energy Procedia. 46 (2014) 194–203. https://doi.org/10.1016/j.egypro.2014.01.173.

[57] L.F. Arenas, C. Ponce de León, F.C. Walsh, Pressure drop through platinized titanium porous electrodes for cerium-based redox flow batteries, 2018. https://doi.org/10.1002/aic.16000.

[58] H. Yang, T.S. Zhao, Q. Ye, Pressure drop behavior in the anode flow field of liquid feed direct methanol fuel cells, J. Power Sources. 142 (2005) 117–124. https://doi.org/10.1016/j.jpowsour.2004.09.036.

[59] C.Y. Ling, H. Cao, M.L. Chng, M. Han, E. Birgersson, Pulsating electrolyte flow in a full vanadium redox battery, J. Power Sources. 294 (2015) 305–311. https://doi.org/10.1016/j.jpowsour.2015.06.020.

[60] W. Xiao, L. Tan, Control strategy optimization of electrolyte flow rate for all vanadium redox flow battery with consideration of pump, Renew. Energy. 133 (2019) 1445–1454. https://doi.org/10.1016/j.renene.2018.09.018.

[61] V. Viswanathan, A. Crawford, D. Stephenson, S. Kim, W. Wang, B. Li, G. Coffey, E. Thomsen, G. Graff, P. Balducci, M. Kintner-Meyer, V. Sprenkle, Cost and performance model for redox flow batteries, J. Power Sources. 247 (2014) 1040–1051. https://doi.org/10.1016/j.jpowsour.2012.12.023.

[62] X. Ke, J.M. Prahl, J.I.D. Alexander, R.F. Savinell, Redox flow batteries with serpentine flow fields: Distributions of electrolyte flow reactant penetration into the porous carbon electrodes and effects on performance, J. Power Sources. 384 (2018) 295–302. https://doi.org/10.1016/j.jpowsour.2018.03.001.

[63] A.A. Shah, H. Al-Fetlawi, F.C. Walsh, Dynamic modelling of hydrogen evolution effects in the all-vanadium redox flow battery, Electrochim. Acta. 55 (2010) 1125–1139. https://doi.org/10.1016/j.electacta.2009.10.022.

[64] Z. Xu, J. Wang, S.C. Yan, Q. Fan, P.D. Lund, Modeling of Zinc Bromine redox flow battery with application to channel design, J. Power Sources. 450 (2020) 227436. https://doi.org/10.1016/j.jpowsour.2019.227436.

[65] A. Trovò, P. Alotto, M. Giomo, F. Moro, M. Guarnieri, A validated dynamical model of a kW-class Vanadium Redox Flow Battery, Math. Comput. Simul. (2020). https://doi.org/10.1016/j.matcom.2019.12.011.

[66] F.T. Wandschneider, D. Finke, S. Grosjean, P. Fischer, K. Pinkwart, J. Tübke, H. Nirschl, Model of a vanadium redox flow battery with an anion exchange membrane and a Larminie-correction, J. Power Sources. 272 (2014) 436–447. https://doi.org/10.1016/j.jpowsour.2014.08.082.

[67] X.L. Zhou, T.S. Zhao, L. An, Y.K. Zeng, L. Wei, Modeling of ion transport through a

porous separator in vanadium redox flow batteries, J. Power Sources. 327 (2016) 67–76. https://doi.org/10.1016/j.jpowsour.2016.07.046.

[68] Y.A. Gandomi, D.S. Aaron, T.A. Zawodzinski, M.M. Mench, In Situ Potential Distribution Measurement and Validated Model for All-Vanadium Redox Flow Battery, J. Electrochem. Soc. 163 (2016) A5188–A5201. https://doi.org/10.1149/2.0211601jes.

[69] X. Ma, H. Zhang, F. Xing, A three-dimensional model for negative half cell of the vanadium redox flow battery, Electrochim. Acta. 58 (2011) 238–246. https://doi.org/10.1016/j.electacta.2011.09.042.

[70] C. Yin, Y. Gao, S. Guo, H. Tang, A coupled three dimensional model of vanadium redox flow battery for flow field designs, Energy. 74 (2014) 886–895. https://doi.org/10.1016/j.energy.2014.07.066.

[71] C. Yin, Y. Gao, G. Xie, T. Li, H. Tang, Three dimensional multi-physical modeling study of interdigitated flow field in porous electrode for vanadium redox flow battery, J. Power Sources. 438 (2019) 227023. https://doi.org/10.1016/j.jpowsour.2019.227023.

[72] X. Ke, J.I.D. Alexander, J.M. Prahl, R.F. Savinell, Flow distribution and maximum current density studies in redox flow batteries with a single passage of the serpentine flow channel, J. Power Sources. 270 (2014) 646–657. https://doi.org/10.1016/j.jpowsour.2014.07.155.

[73] H. Chen, X. Li, H. Gao, J. Liu, C. Yan, A. Tang, Numerical modelling and in-depth analysis of multi-stack vanadium flow battery module incorporating transport delay, Appl. Energy. 247 (2019) 13–23. https://doi.org/10.1016/j.apenergy.2019.04.034.

[74] G. Aparicio-Mauricio, F.A. Rodríguez, J.J.H. Pijpers, M.R. Cruz-Díaz, E.P. Rivero, CFD modeling of residence time distribution and experimental validation in a redox flow battery using free and porous flow, J. Energy Storage. 29 (2020) 101337. https://doi.org/10.1016/j.est.2020.101337.

[75] P.A. García-Salaberri, T.C. Gokoglan, S.E. Ibáñez, E. Agar, M. Vera, Modeling the effect of channel tapering on the pressure drop and flow distribution characteristics of interdigitated flow fields in redox flow batteries, Processes. 8 (2020) 775. https://doi.org/10.3390/PR8070775.

[76] B.W. Zhang, Y. Lei, B.F. Bai, A. Xu, T.S. Zhao, A two-dimensional mathematical model for vanadium redox flow battery stacks incorporating nonuniform electrolyte distribution in the flow frame, Appl. Therm. Eng. 151 (2019) 495–505. https://doi.org/10.1016/j.applthermaleng.2019.02.037.

[77] H. Ishitobi, J. Saito, S. Sugawara, K. Oba, N. Nakagawa, Visualized cell characteristics by a two-dimensional model of vanadium redox flow battery with interdigitated channel and thin active electrode, Electrochim. Acta. 313 (2019) 513–522. https://doi.org/10.1016/j.electacta.2019.04.055.

[78] X. Ke, J.M. Prahl, J.I.D. Alexander, R.F. Savinell, Mathematical Modeling of Electrolyte Flow in a Segment of Flow Channel over Porous Electrode Layered System in Vanadium Flow Battery with Flow Field Design, Electrochim. Acta. 223 (2017) 124–134. https://doi.org/10.1016/j.electacta.2016.12.017.

[79] F.F. Rivera, B. Miranda-Alcántara, G. Orozco, C. Ponce de León, L.F. Arenas, Pressure drop analysis on the positive half-cell of a cerium redox flow battery using computational

fluid dynamics: Mathematical and modelling aspects of porous media, Front. Chem. Sci. Eng. (2020) 1–11. https://doi.org/10.1007/s11705-020-1934-9.

[80] D. Zhang, A. Forner-Cuenca, O.O. Taiwo, V. Yufit, F.R. Brushett, N.P. Brandon, S. Gu, Q. Cai, Understanding the role of the porous electrode microstructure in redox flow battery performance using an experimentally validated 3D pore-scale lattice Boltzmann model, J. Power Sources. 447 (2020) 227249. https://doi.org/10.1016/j.jpowsour.2019.227249.

[81] W.W. Yang, Y.L. He, Y.S. Li, Performance Modeling of a Vanadium Redox Flow Battery during Discharging, Electrochim. Acta. 155 (2015) 279–287. https://doi.org/10.1016/j.electacta.2014.12.138.

[82] M. MacDonald, R.M. Darling, Modeling flow distribution and pressure drop in redox flow batteries, AIChE J. 64 (2018) 3746–3755. https://doi.org/10.1002/aic.16330.

[83] M. Macdonald, R.M. Darling, Comparing velocities and pressures in redox flow batteries with interdigitated and serpentine channels, AIChE J. 65 (2019) 1–11. https://doi.org/10.1002/aic.16553.

[84] R. Badrinarayanan, K.J. Tseng, B.H. Soong, Z. Wei, Modelling and control of vanadium redox flow battery for profile based charging applications, Energy. 141 (2017) 1479–1488. https://doi.org/10.1016/j.energy.2017.11.082.

[85] Z. Wei, J. Zhao, M. Skyllas-Kazacos, B. Xiong, Dynamic thermal-hydraulic modeling and stack flow pattern analysis for all-vanadium redox flow battery, J. Power Sources. 260 (2014) 89–99. https://doi.org/10.1016/j.jpowsour.2014.02.108.

[86] X. Ke, J.I.D. Alexander, J.M. Prahl, R.F. Savinell, A simple analytical model of coupled single flow channel over porous electrode in vanadium redox flow battery with serpentine flow channel, J. Power Sources. 288 (2015) 308–313. https://doi.org/10.1016/j.jpowsour.2015.04.138.

[87] P.A. Ramachandran, Advanced Transport Phenomena, Cambridge University Press, 2014. https://doi.org/10.1017/CBO9780511980527.

[88] J. Bear, Dynamics of Fluids in Porous Media, Dover Publications, New York, 1973.

[89] D. Ruth, H. Ma, On the Derivation of the Forchheimer Equation by Means of the Averaging Theorem, Kluwer Academic Publishers, 1992.

[90] D.A. Nield, A. Bejan, Convection in porous media, 3rd ed., Springer, 2006.

[91] H. Ma, D.W. Ruth, The microscopic analysis of high forchheimer number flow in porous media, Transp. Porous Media. 13 (1993) 139–160. https://doi.org/10.1007/BF00654407.

[92] S. Whitaker, The Forchheimer equation: A theoretical development, Transp. Porous Media. 25 (1996) 27–61. https://doi.org/10.1007/BF00141261.

[93] D.D. Joseph, D.A. Nield, G. Papanicolaou, Nonlinear equation governing flow in a saturated porous medium, Water Resour. Res. 18 (1982) 1049–1052. https://doi.org/10.1029/WR018i004p01049.

[94] H.C. Brinkman, A calculation of the viscous force exerted by a flowing fluid on a dense swarm of particles, Flow, Turbul. Combust. 1 (1949) 27. https://doi.org/10.1007/BF02120313.

[95] F.J. Valdes-Parada, J.A. Ochoa-Tapia, J. Alvarez-Ramirez, On the effective viscosity for

the Darcy-Brinkman equation, Physica A. 385 (2007) 69–79. https://doi.org/10.1016/j.physa.2007.06.012.

[96] M. Kapoor, R.K. Gautam, V.K. Ramani, A. Verma, Predicting operational capacity of redox flow battery using a generalized empirical correlation derived from dimensional analysis, Chem. Eng. J. 379 (2020) 122300. https://doi.org/10.1016/j.cej.2019.122300.

[97] B. Mukherjee, B.A. Wrenn, P. Ramachandran, Relationship between size of oil droplet generated during chemical dispersion of crude oil and energy dissipation rate: Dimensionless, scaling, and experimental analysis, Chem. Eng. Sci. 68 (2012) 432–442. https://doi.org/10.1016/j.ces.2011.10.001.

[98] E. Ruckenstein, Analysis of transport phenomena using scaling and physical models, Adv. Chem. Eng. 13 (1987) 11–112. https://doi.org/10.1016/S0065-2377(08)60016-2.

[99] Z. Wang, S. Sankarasubramanian, V. Ramani, Reactant-Transport Engineering Approach to High-Power Direct Borohydride Fuel Cells, Cell Reports Phys. Sci. 1 (2020) 100084. https://doi.org/10.1016/j.xcrp.2020.100084.

[100] Q. Ye, T.X. Shan, P. Cheng, Thermally induced evolution of dissolved gas in water flowing through a carbon felt sample, Int. J. Heat Mass Transf. 108 (2017) 2451–2461. https://doi.org/10.1016/j.ijheatmasstransfer.2017.01.097.

[101] B.R. Munson, D.F. Young, T.H. Okiishi, Fundamentals of fluid mechanics, (1994). https://doi.org/10.1016/b978-0-12-800944-4.00002-0.

[102] DOE FUNDAMENTALS HANDBOOK, Thermodynamics, Heat Transfer and Fluid Flow, US Department of Energy, 1992.

[103] R.M. Darling, M.L. Perry, The Influence of Electrode and Channel Configurations on Flow Battery Performance, J. Electrochem. Soc. 161 (2014) A1381–A1387. https://doi.org/10.1149/2.0941409jes.

[104] SERIES 4000 CAPSUHELIC ®-MODELS AND RANGES, (n.d.). http://www.bbinstruments.com/downloads/Dwyer_4000.pdf (accessed February 18, 2021).

[105] J.L. Meriam, L.G. Kraige, J.N. Bolton, Engineering Mechanics: Statics, 9th ed., 2018. https://www.wiley.com/en-us/Engineering+Mechanics%3A+Statics%2C+9th+Edition-p-9781119392620 (accessed February 18, 2021).